Heterogeneous complement and microglia activation mediates stress-induced synapse loss

Authors: Breeanne M. Soteros[1], Haven Tillmon[1], Mackenna Wollet[2], Julianne General[1], Hanna Chin[5], John Beichen Lee[3], Flavia R. Carreno[1], David A. Morilak[1,4], Jun Hee Kim[2,6], Gek Ming Sia[1*]

Affiliations: [1]Department of Pharmacology, [2]Department of Cellular and Integrative Physiology, [3]Long School of Medicine, University of Texas Health at San Antonio, San Antonio, TX 78229, [4]South Texas Veteran's Health Care System, San Antonio, TX 78229, [5]University of Rochester, Rochester, NY 14627, [6]Kresge Hearing Research Institute, University of Michigan, Ann Arbor, MI 48109

*Correspondence to siag@uthscsa.edu

Abstract

Spatially heterogeneous synapse loss is a characteristic of many psychiatric and neurological disorders, but the underlying mechanisms are unclear. Here, we show that spatially-restricted complement activation mediates stress-induced heterogeneous microglia activation and synapse loss localized to the upper layers of the mouse medial prefrontal cortex (mPFC). Single cell RNA sequencing also reveals a stress-associated microglia state marked by high expression of the apolipoprotein E gene ($ApoE^{high}$) localized to the upper layers of the mPFC. Mice lacking complement component C3 are protected from stress-induced layer-specific synapse loss, and the $ApoE^{high}$ microglia population is markedly reduced in the mPFC of these mice. Furthermore, C3 knockout mice are also resilient to stress-induced anhedonia and working memory behavioral deficits. Our findings suggest that region-specific complement and microglia activation can contribute to the disease-specific spatially restricted patterns of synapse loss and clinical symptoms found in many brain diseases.

Introduction

Synapse loss is a central mechanism that plays an important role in the pathogenesis of many psychiatric and neurological diseases[1–6]. Neuroimaging and neuropathological studies have revealed disease-specific and reproducible spatial patterns of synapse loss in many brain disorders[7–10]. In some neuropsychiatric diseases, severe synapse loss can occur in remarkably small brain regions, while nearby regions are spared. For example, postmortem studies of schizophrenic patients show a consistent loss of dendritic spines in layer 3 of the dorsolateral prefrontal cortex (PFC)[11,12], while spine density in deeper PFC layers[13] and other cortical regions[14] are unaffected. Studies of rodent models of depression also show that dendritic spines in the upper layers of the medial PFC (mPFC) are lost in response to stress, while spines in the deeper mPFC layers remain unaffected[15,16]. Despite the prevalence of region-specific synapse loss in brain diseases, the pathophysiological processes involved remain unclear.

Microglia are dynamic brain-resident macrophages that constantly survey their environment and respond to a wide variety of pathological insults. Single cell-RNA sequencing studies have revealed that under physiological conditions, microglia adopt diverse regional states dictated by their local environment[17–20]. A large number of pathological and spatially heterogeneous microglial transcriptomic states have also been described diseases such as Alzheimer's disease[21–23], multiple sclerosis[19,24,25], and chronic pain[26]. These diverse microglia states are likely to perform key homeostatic functions in the healthy brain and play critical pathogenic roles in the diseased brain. While several signaling pathways have been shown to induce specific pathological microglial states[27–30], whether these mechanisms act in a spatially-restricted manner remain unclear.

Stress is a major risk factor for psychiatric diseases, and extended periods of stress can directly cause affective disorders such as major depressive disorder (MDD)[31], post-traumatic stress disorder (PTSD)[32,33], and anxiety disorders[32,33]. Extended periods of stress also cause synapse loss in the PFC, an effect which is mediated by glucocorticoid stress hormones. Excessive secretion of cortisol is found in 50% of depressed patients[34], and levels of cortisol are positively correlated to depressive behavior in non-human primates[35]. In humans, elevated salivary, hair and serum cortisol levels are all correlated with poorer working memory performance and lower brain volumes[36–39], suggesting that prolonged exposure to cortisol can lead to changes in brain structure. Chronic stress is known to increase microglia activation in the PFC[40,41], and can also induce complement activation in the brain[42–44], suggesting that microglial phagocytosis of synapses may mediate stress-induced synapse loss. However, previous studies have assumed that stress-induced microglia activation occurs homogeneously throughout the PFC. Because the complement cascade is a secreted and extracellular signaling system, it was unclear whether this signaling pathway can result in spatially-restricted microglia activation and synapse loss in the brain.

Here, we provide evidence that chronic stress causes heterogeneous microglia activation in the mPFC resulting in layer-specific synapse loss and stress-associated behavioral deficits. We show

that multiple chronic stress protocols cause localized complement activation specifically in the upper layers of the mouse mPFC. Complement activation in layer 2/3 leads to microglial phagocytosis of VGlut2 synapses and synapse loss specifically in those cortical layers, while synapses in deeper mPFC layers are spared. Single-cell RNA (scRNA-seq) of microglia from cortices of stressed mice also reveals an ApoE^{high} transcriptomic state upregulated in the stressed brain and localized to layer 2/3 of the mPFC. In complement C3 knockout (KO) mice, we found that chronic stress no longer induces the ApoE^{high} microglia state. C3 KO mice are also resilient to stress-induced microglia phagocytosis of synapses and synapse loss, and do not exhibit stress-induced anhedonia and working memory deficits. Our data shows that spatially restricted complement activation can drive heterogeneous activation of microglia to cause layer-specific synapse loss in the stressed mPFC.

Results

Multiple stress protocols cause layer-specific complement activation in the mPFC

The classical complement cascade is a major signaling pathway that mediates microglial phagocytosis of synapses[45–47]. Complement component C3, the main effector molecule in the complement cascade, is deposited onto synapses and recognized by microglial CR3 receptors for phagocytosis[45]. To determine whether chronic stress induces heterogeneous complement activation, we subjected C57BL/6J mice to the 21-day chronic corticosterone (CORT) administration protocol (Figure 1A), and assessed complement activation in the mPFC by staining for C3. We focused on the prelimbic cortex of the mPFC (Figure 1B), a region known to be especially sensitive to the effects of stress[48]. Surprisingly, we found that CORT treatment causes a layer-specific increase in C3 deposition in layer 2/3 of the mPFC but not layer 5/6 (Figures 1C-E). The effects of stress on neuroimmune processes can vary depending on the stressor used[49], raising the question of whether layer-specific complement activation is a core feature of diverse stressors. In order to determine whether layer-specific complement activation also occurs in other stressors, we assessed C3 deposition in two other commonly used stress protocols, chronic restraint stress (CRS), and chronic unpredictable stress (CUS). Both of these protocols engage the fast autonomic nervous system (ANS) response, in addition to the slow hypothalamic-pituitary-adrenal (HPA) axis hormonal response that the CORT protocol mimics. Both of these protocols also provide different patterns of CORT responses. CRS is expected to cause an initial large increase in CORT levels which habituates over time, whereas CUS is designed to cause a non-habituating increase in CORT levels. Surprisingly, both CRS and CUS cause a layer-specific increase in C3 deposition similar to that found in chronic CORT administration (Figures 1F-K), despite differences in the physiological systems engaged and patterns of CORT induced by these protocols. Therefore, multiple chronic stress protocols lead to layer-specific complement activation in the mPFC, suggesting that layer-specific complement activation is a core feature of chronic stress.

110 **Stress causes layer-specific microglial synapse phagocytosis and synapse loss**

111 Complement activation is known to lead to microglial activation and phagocytosis of synapses[45].
112 To further characterize microglia in the context of chronic stress, we chose to perform all further
113 experiments with the CORT stress protocol, because CORT is the principal murine stress
114 hormone, and CORT levels are increased by all rodent stress protocols[50–52]. Furthermore, direct
115 CORT administration causes synapse losses and behavioral deficits in rodents[53–57], and
116 glucocorticoid receptor blockade in rodents block stress-induced microglia activation, neuronal
117 remodeling, and behavioral deficits[57], indicating that CORT is necessary and sufficient for the
118 neurobiological effects of chronic stress. To assess microglial activation, we stained brain slices
119 for the microglial cytoplasmic marker Iba1 and the lysosomal marker CD68 (Figure 2A),
120 reconstructed high resolution 3D images of individual microglia, and quantitated the percentage
121 of Iba1 volume occupied by CD68 lysosomes. We found that the CD68 content of microglia is
122 increased by chronic CORT administration only in layer 2/3 (Figure 2B), while microglia in
123 layer 5 are not affected (Figure 2C). Previous studies have shown that chronic CORT
124 administration causes synapse loss in the mPFC[53–55]. Furthermore, live imaging studies indicate
125 that stress-induced synapse loss in the mPFC is due to an increase in the rate of synapse
126 elimination[54,58,59], as opposed to a decrease in the rate of synapse formation, suggesting that
127 microglial synapse phagocytosis may be involved. To assess microglial synapse phagocytosis in
128 the mPFC of chronically stressed mice, we stained their brain slices for Iba1, CD68, and the
129 presynaptic marker VGlut2. We chose VGlut2 because studies from our lab and others have
130 shown that microglia preferentially phagocytose this population of synapses[45,46,60]. We
131 quantitated the 3D colocalization of the three markers Iba1/CD68/VGlut2 as a measure of
132 microglial synapse phagocytosis (Figure 2D), and found that chronic CORT administration
133 strongly increases microglial synapse phagocytosis in layer 2/3 of the mPFC, but not in layer 5/6
134 (Figures 2E-F).

135 To determine if the increase in microglial synapse phagocytosis leads to a decrease in synapse
136 density in the stressed mPFC, we stained brain slices for three types of synapses: 1)
137 thalamocortical synapses marked by colocalized VGlut2 presynaptic and PSD95 postsynaptic
138 markers, 2) corticocortical synapses marked by colocalized VGlut1 presynaptic and PSD95
139 postsynaptic markers, and 3) inhibitory synapses marked by colocalized VGAT presynaptic and
140 gephyrin postsynaptic markers. We found that chronic CORT administration results in a layer-
141 specific reduction of VGlut2/PSD95 synapses in layer 2/3, but not layer 5 (Figures 2G-H), while
142 the densities of VGlut1/PSD95 and VGAT/gephyrin synapses are unchanged in all cell layers
143 (Figures 2I-L). These findings suggest that microglial synapse phagocytosis induced by chronic
144 CORT administration specifically targets thalamocortical synapses in layer 2/3 of the mPFC,
145 while sparing corticocortical and inhibitory synapses.

146 Activity of the thalamic projections to the PFC is known to be required for working memory
147 performance, where it acts to sustain the delay-period activity of PFC neurons which are the
148 neuronal substrates of working memory maintenance[61–63]. Chronic stress is also known to impair

149 thalamic inputs to the mPFC and working memory performance in mice[56,57,64]. To determine
150 whether stress-induced loss of synapses in the mPFC results in a layer-specific reduction of
151 functional activation of neurons during working memory maintenance, we utilized the temporal
152 object recognition (TOR) working memory task, which has previously been shown to be
153 impaired by chronic stress in mice[56,57]. We assessed the number of c-fos positive neurons in the
154 mPFC shortly after the completion of the TOR task, and found a significant reduction in layer
155 2/3 of the mPFC from CORT mice, but not in layer 5/6 (Figures 2M-O). Together, these data
156 indicate that chronic CORT causes heterogeneous microglia activation in the mPFC leading to
157 layer-specific synapse loss.

158

159 **Stress induces an ApoE^{high} microglia state enriched in endocytotic genes**

160 To characterize the heterogeneous states of microglia in the stressed brain, we performed
161 scRNA-seq on microglia isolated from the brains of CORT and control mice. To isolate single
162 cell microglia from the gray matter of mouse cortex, we used a cold mechanical dissociation
163 protocol that was specifically optimized for the isolation of microglia with minimal *ex vivo*
164 transcriptional alterations (Figure 3A)[19,65]. After dissociation, microglia were sorted from the
165 single cell suspension with fluorescence activated cell sorting (FACS) based on expression of
166 Cd45, Cd11b, and Cx3cr1. (Supplementary Figure 1). The resulting cells were processed for
167 single cell RNA sequencing, and sequenced to a depth of more than 50,000 reads/cell. We
168 processed 2 replicates each for the control and CORT conditions, with 4 mice per replicate. After
169 quality control, we retained a total of 35,292 cells from all replicates for downstream analysis.

170 We then performed unsupervised clustering analysis on the single scRNA-seq dataset, revealing
171 5 clusters across all conditions and replicates (Figure 3B). We analyzed each cluster for
172 differentially expressed genes (DEGs), and annotated each cluster with its most highly expressed
173 DEG, with the exception of the largest cluster, which we termed the homeostatic cluster (Figures
174 3C, D). In accordance with previous reports, adult microglia are largely homogeneous and are
175 mostly in the homeostatic state (Figures 3B, C)[18,19,65]. Chronic CORT administration
176 dramatically increases the number of microglia in the ApoE^{high} state in both CORT biological
177 replicates (Figures 3C, D), while decreasing the number of homeostatic microglia. Compared to
178 the homeostatic state, the ApoE^{high} microglia state exhibits greatly increased expression of the
179 ApoE gene, with a nearly 32-fold increase over the homeostatic state, as well as increases in the
180 expression of several Ms4a genes (Figure 4D). Intriguingly, both ApoE and Ms4a genes are
181 associated with AD risk[66–68], suggesting a microglia-dependent mechanism for acceleration of
182 AD progression by stress. In addition to the homeostatic and ApoE^{high} cell clusters, we also
183 identified several smaller cell clusters which are largely unchanged by chronic CORT
184 administration (Figures 3C, D), many of which have already been identified in previous
185 microglia scRNA-seq studies[65,69,70], suggesting that they are microglia states present in basal
186 conditions. These clusters include an interferon-responsive state marked by expression of Ifitm3
187 and other interferon-responsive genes[65,70], and a chemokine-expressing state marked by Ccl4 and

188 other chemokine expression (Figures 3B, C)[65,69]. We also identified a microglia state marked by
189 expression of the protein kinase Prkg1, which to our knowledge has not been previously
190 described (Figures 3B, C). All cell clusters express canonical microglial genes such as C1qa,
191 Cx3cr1, P2ry12, and Tmem119 (Figure 4A), indicating that they are *bona fide* microglia states.

192 Chronic CORT administration increases the number of microglia in the ApoE^{high} state while
193 decreasing the number of homeostatic microglia (Figures 3B, C), suggesting that CORT induces
194 microglia to convert from the homeostatic state to the ApoE^{high} state. To identify the genes
195 involved in this transition, we performed pseudotime trajectory analysis on the dataset. This
196 analysis corroborated that the homeostatic population transitioned to the ApoE^{high} population
197 along a single trajectory (Figure 4E), and that 93 genes were differentially expressed along this
198 trajectory, including the ApoE gene (Figure 4F). We then performed gene set enrichment
199 analysis (GSEA) on the 93 genes, which showed that genes associated with receptor mediated
200 endocytosis were significantly enriched among these genes (Figure 4G). In addition, genes
201 associated with negative regulation of T cell activation and antigen presentation were also
202 differentially expressed in microglia (Figure 4G), consistent with the known immunosuppressive
203 function of the glucocorticoids. The enrichment of genes involved in receptor mediated
204 endocytosis suggests that ApoE^{high} microglia are primed for phagocytosis by stress.

205

206 **Complement activation drives formation of ApoE^{high} microglia state**

207 Next, we wanted to determine if layer-specific complement activation resulted in layer-specific
208 induction of ApoE^{high} microglia in the mPFC. We mapped ApoE-expressing microglia in the
209 mPFC, using RNAscope *in situ* hybridization (ISH) to probe for both Cx3cr1 mRNA transcripts
210 as a microglia marker, and ApoE transcripts as the readout. We took a semi-quantitative
211 approach that was suggested by the manufacturer, categorizing Cx3cr1-positive microglia into
212 bins based on their ApoE mRNA content, ranging from no expression (bin 0) to high expression
213 (bin 4) (Figure 5A). We then characterized the bin distribution for ApoE expression in wildtype
214 and C3$^{-/-}$ mice treated with control or CORT (Figures 5B-E). Notably, in wildtype mice treated
215 with CORT, over 25% of all microglia in layer 2/3 are bin 4 ApoE^{high} microglia, whereas less
216 than 10% of microglia in control mice are bin 4 ApoE^{high} (Figures 5B, D). This dramatic increase
217 in ApoE^{high} microglia population is not seen in layer 5 (Figures 5C, E). In addition, C3 deletion
218 abolishes the layer-specific increase in ApoE^{high} microglia (Figures 5B-E). These data suggest
219 that complement activation drives the formation of the ApoE^{high} microglia state.

220

221 **Complement activation drives stress-induced synapse loss and behavioral deficits**

222 To determine if C3 deletion leads to a lack of stress-induced microglial and synaptic responses,
223 we next assessed VGlut2/PSD95 synapse density and microglial phagocytosis of VGlut2
224 synapses in the mPFC of control and CORT-treated C3$^{-/-}$ mice (Figures 6A, B). We found that
225 mice lacking C3 were protected against CORT-induced microglial phagocytosis of synapses and

synapse loss in layer 2/3 (Figures 6C-F). These data indicate that stress-induced layer-specific changes in microglial synapse phagocytosis and synapse density are abolished in the $C3^{-/-}$ mice.

Finally, we wanted to determine if C3 deletion also leads to the rescue of behavioral deficits. We assessed $C3^{-/-}$ and wildtype mice in two behavioral tasks, the SPT task for anhedonia, and the TOR task for working memory (Figures 7A, B). We found that wildtype mice, but not $C3^{-/-}$ mice, were susceptible to CORT-induced anhedonia in the SPT task (Figure 7C). In addition, we found that wildtype mice but not $C3^{-/-}$ mice were susceptible to CORT-induced impairments in working memory. Specifically, we found that control-treated wildtype mice and CORT/control-treated $C3^{-/-}$ mice were able to remember objects they have recently encountered, as shown by their preferential exploration of the old and more unfamiliar object. In contrast, CORT-treated wildtype mice had impaired working memory and explored both old and recent objects equally (Figures 7D, E). Therefore, our data indicate that $C3^{-/-}$ mice are resilient against stress-induced anhedonia and working memory deficits. Taken together, our findings indicate that stress-induced layer-specific complement activation in the mPFC leads to heterogeneous microglia activation, layer-specific synapse loss and behavioral deficits.

Discussion

In this study, we show that chronic stress causes spatially-restricted complement activation in the upper cortical layers of the mPFC, resulting in local microglia synapse phagocytosis and synapse loss, as well as anhedonia and working memory deficits. Single cell transcriptomics of the stressed cortex show a dramatic upregulation of the ApoE gene in many microglia, with $ApoE^{high}$ microglia also localized to layer 2/3 of the mPFC. Deletion of the C3 gene blocks the stress-induced layer-specific increases in microglial synapse phagocytosis, synapse loss, and $ApoE^{high}$ microglia population in layer 2/3 of the mPFC. Mice lacking the C3 gene are also resilient against stress-induced anhedonia and working memory deficits. Our findings highlight the role of spatially-restricted microglia activation in the brain in mediating the neurological symptoms of stress-associated diseases such as depression, and reveals the potential role of localized complement and microglia activation in causing region-specific synapse loss in other brain diseases.

The PFC plays an important role in the complex cognitive control of many behaviors, including the regulation of emotion and working memory. During brain development, the PFC is the last region to mature, with an extended developmental period spanning decades in humans[71,72], making the PFC vulnerable to many environmental and genetic insults. Recent studies indicate that the upper layers of the PFC are preferentially affected in many psychiatric and neurological diseases. Neuropathological studies of brains from schizophrenic patients show a consistent loss of dendritic spines in layer 3 of the dorsolateral PFC[11,12], while spine density in deeper PFC layers[13] and other cortical regions[14] are unaffected. A transcriptomics study of brain cells from autistic patients has also shown that specific sets of genes enriched in neurons and microglia in the upper layers of the PFC are correlated with clinical severity[73]. In Alzheimer's disease (AD),

265 postmortem brain studies have revealed high Aβ plaque densities in PFC layers 2/3[74–76], and
266 increased numbers of reactive astrocytes in the same layers[77]. Here, we show that layer 2/3 of the
267 mPFC is selectively vulnerable to stress-induced synapse loss as a result of layer-specific
268 complement and microglia activation. Our findings suggest that the selective vulnerability of the
269 upper layers of the PFC in many brain diseases is based on a propensity for runaway complement
270 activation, although the exact molecular mechanisms and cell types involved remain to be
271 determined.

272 Many studies have shown that microglia are exquisitely sensitive to the environment. A recent
273 single cell transcriptomic study of microglia has shown that in the somatosensory cortex,
274 microglia adopt layer-specific transcriptional states that are determined by signals from
275 laminarly distributed pyramidal neurons[17]. Therefore, a straightforward mechanism for layer-
276 specific complement activation is the stress-induced increase in the expression of complement
277 components or activators in a particular neuronal or astrocytic layer[78] in the mPFC.
278 Alternatively, a stress-induced decrease in the expression of complement inhibitors[46,79,80] within
279 the upper layers can also lead to regional complement activation. In addition, inputs into the
280 mPFC are known to be layer-specific[81], and a stress-induced signals emanating from specific
281 presynaptic terminals that are laminarly distributed may also trigger layer-specific complement
282 and microglia activation. The above hypothetical mechanisms are not mutually exclusive and
283 may span more than one cell type, and further investigation is required to fully elucidate the
284 mechanisms involved.

285 In addition to showing that stress induces layer-specific complement and microglia activation,
286 our scRNA-seq data also revealed a stress-induced ApoE^{high} microglia state. We speculate that
287 the ApoE^{high} microglia population phagocytoses synapses in layer 2/3 of the mPFC based on the
288 following lines of evidence: 1) GSEA analysis on the ApoE^{high} microglia state indicate an
289 enrichment of endocytotic genes, suggesting that these microglia perform a phagocytic function;
290 2) both the ApoE^{high} microglia and the microglia shown immunohistologically to be
291 phagocytosing synapses are localized to layer 2/3, suggesting that they are the same population
292 of microglia, and 3) both the ApoE^{high} microglia and the microglia that phagocytose synapses are
293 ablated by C3 gene deletion, again arguing that they are the same microglia population.
294 However, we acknowledge that these lines of evidence are indirect. We are unable to directly use
295 ApoE as an immunohistological marker for ApoE^{high} microglia because ApoE is also secreted by
296 astrocytes and are avidly phagocytosed by all microglia (data not shown), rendering ApoE
297 staining unreliable as a marker for ApoE^{high} microglia. We were also unable to identify
298 additional genes that simultaneously label the entirety of the ApoE^{high} microglia population and
299 were detectable by high quality antibodies, which precluded the use of alternative markers.
300 Furthermore, the ISH process for detecting ApoE transcripts is moderately destructive on brain
301 slices, and renders them unsuitable for the synapse phagocytosis assay. Therefore, as a result of
302 technical issues, we are unable to directly demonstrate a synapse phagocytosis function for the
303 ApoE^{high} microglia. In addition, it is possible that the ApoE^{high} microglia population may
304 perform other functions, such as cytokine secretion, that are not detected by the DEG and GSEA

305 analyses due to the relatively low sensitivity of the 10x Genomics scRNA-seq platform for low
306 copy number mRNA. Therefore, further work is required to elucidate the biological functions of
307 the stress-induced ApoE^{high} microglia state.

308 Numerous scRNA-seq studies have shown that microglia adopt disease-associated transcriptomic
309 states. Intriguingly, many of these states include the upregulation of the ApoE gene. Examples of
310 ApoE-associated microglial states include the disease-associated microglia (DAMs) found in
311 AD[21,27], human AD microglia (HAMs)[82], the microglial neurodegenerative phenotype (MGnD)
312 found in mouse models of AD/ALS/MS[24], microglia found in peripheral nerve injury and chronic
313 pain[26], activated response microglia (ARMs) found in aged mice and an AD mouse model[83],
314 microglia inflamed in MS (MIMS)[25], and a microglia state associated with injury[19]. The
315 upregulation of microglial ApoE in a wide variety of diseases suggests that ApoE upregulation is
316 part of a generic microglial response to tissue damage. Interestingly, early studies in stress
317 biology describe the stress response as a "general adaptation syndrome" that occurs in diverse
318 diseases[84,85]. In this study, we show that the stress hormone corticosterone induces an ApoE^{high}
319 microglia state, suggesting that the ApoE component of multiple disease-associated microglial
320 states may be a result of stress hormone release in those diseases.

321 Stress is also known to aggravate or trigger the occurrence of other neurological and psychiatric
322 diseases. For example, stress is known to trigger episodes of psychosis in schizophrenic
323 patients[86,87] and attacks in multiple sclerosis patients[88], as well as accelerate the progression of
324 AD[89–91]. All of these diseases are associated with aberrant complement activation in the
325 brain[25,92–99]. Our findings suggest that stress may aggravate these diseases through additive
326 complement and microglia activation. We also show that only VGlut2 synapses in layer 2/3
327 mPFC are phagocytosed by microglia, while VGlut1 and VGAT synapses are spared, indicating
328 that even within a region of complement activation, specific microcircuits may be selectively
329 impaired. These findings may be relevant when assessing the neural circuits involved in various
330 complement-associated brain diseases.

331 Neuroimaging studies have revealed disease-specific and reproducible patterns of gray matter
332 volume (GMV) reductions in many brain diseases, including depression[100–102], schizophrenia[103],
333 and other major psychiatric diseases[104,105]. A more recent study has showed that substantial
334 heterogeneity also exists in the individual pattern of GMV changes in patients diagnosed with the
335 same psychiatric disorder, and suggests that individual variation in disease symptoms may be a
336 result of this heterogeneity[104]. Other studies have also shown that elevated salivary, hair and
337 serum cortisol levels are all correlated with lower brain volumes[38,39], and that stressful life events
338 leave a replicable pattern of brain volume reductions that is predictive of current and future
339 anxiety[106]. While GMV is a complex measure that encompasses glia, vasculature and neuronal
340 dendritic and synapse volumes, longitudinal studies show a lifetime trajectory of GMV loss[107,108]
341 that temporally correlates with neuropathological studies of dendritic spine loss due to increased
342 synapse pruning during adolescence and early adulthood[109,110], suggesting that synapse loss is a
343 major contributor to GMV reductions. Given the large variation in complement activity found in

344 the human population[111], genetic polymorphisms in complement components and regulators may
345 account for the individual variation in GMV reductions observed in psychiatric patients. Our
346 study suggests that lifetime adversity can leave spatially heterogeneous patterns of brain volume
347 reductions through heterogeneous complement and microglia activation, and that regional
348 regulation of these processes play an important role in the heterogeneity of neuropsychiatric
349 diseases.

350

351 **Acknowledgements**

352 This work is supported by the National Institute of Neurological Disorders and Stroke (NINDS)
353 grant (R01NS112389) to G.M.S., the National Institute on Deafness and other Communication
354 Disorders (NIDCD) grants (R01DC018797, R01DC019371) to J.H.K, the National Institute of
355 Mental Health (NIMH) grant (R01MH053851) to D.A.M., and the NIMH grant
356 (R21MH113899) to F.R.C.. Imaging was performed at UTHSA Optical Imaging Facility, which
357 is supported by a grant from the NCI (P30CA54174). FACS was performed at the Flow
358 Cytometry Shared Resource at UTHSA, which is supported by an NCI grant (P30CA054174) to
359 the Mays Cancer Center, a Cancer Prevention and Research Institute of Texas (CPRIT) grant
360 (RP210126), a National Institutes of Health (NIH) Shared Instrument grant (S10OD030432), and
361 support from the Office of the Vice President for Research at UTHSA. RNA sequencing was
362 performed at the UTHSA Genome Sequencing Facility, which is supported by an NCI grant
363 (P30CA054174), an NIH Shared Instrument grant (S10OD030311), and a CPRIT core facility
364 award (RP220662).

365

366 **Author contributions**

367 G.M.S. and B.M.S. designed the study. B.M.S. carried out most of the anatomical and behavioral
368 experiments. H.T. ,H.C., and J.G. assisted with anatomical and behavioral experiments. M.W.
369 and J.H.K. assisted with neuronal functional experiments. J.B.L. assisted with scRNA-seq
370 analysis. D.A.M. and F.R.C. assisted with the design of the stress protocols. G.M.S. supervised
371 the project. G.M.S. and B.M.S. wrote the manuscript.

372

373 **Declaration of interests**

374 The authors declare no competing interests.

375

376 **Data availability**

377 Single cell RNA sequencing data will be deposited at the Gene Expression Omnibus (GEO) and
378 be publicly available upon publication. All additional data and code will be provided upon
379 request.

380

381 **Figure legends**
382
383 **Figure 1. Multiple stress protocols cause layer-specific complement activation in the mPFC.**

384 (A) Schematic depicting timeline for chronic corticosterone (CORT) stress, chronic restraint
385 stress (CRS), and chronic unpredictable stress (CUS) protocols.

386 (B) Low-magnification image depicting layers of the medial prefrontal cortex. Stained for
387 VGlut2 (red) and DAPI (blue).

388 (C) Low magnification image showing laminar C3 deposition in mPFC in control/CORT mice.
389 Top panel shows C3 channel (white), bottom panel shows merged C3 (red) and DAPI (blue)
390 channels. Scale bar 50 µm.

391 (D) Quantitation (left) and representative image (right) of C3 deposition in layer 2/3 mPFC after
392 control/CORT. Analyzed by two-tailed unpaired t-test, t(13)=2.394, *p=0.0325, n=7-8 from
393 3-4 mice. All data shown as mean ± s.e.m.. Scale bar 5 µm.

394 (E) Quantitation (left) and representative image (right) of C3 deposition in layer 5 mPFC after
395 control/CORT. Analyzed by two-tailed unpaired t-test, t t(14)=0.6462, p=0.5286, n=8 from 4
396 mice. All data shown as mean ± s.e.m.. Scale bar 5 µm.

397 (F) Low magnification image showing laminar C3 deposition in mPFC in control/CRS mice.
398 Top panel shows C3 channel (white), bottom panel shows merged C3 (red) and DAPI (blue)
399 channels. Scale bar 50 µm.

400 (G) Quantitation (left) and representative image (right) of C3 deposition in layer 2/3 mPFC after
401 control/CRS. Analyzed by two-tailed unpaired t-test, t(5)=5.491, **p=0.0027, n=3-4 mice.
402 All data shown as mean ± s.e.m.. Scale bar 5 µm.

403 (H) Quantitation (left) and representative image (right) of C3 deposition in layer 5 mPFC after
404 control/CRS. Analyzed by two-tailed unpaired t-test, t(5)=0.7149, p=0.5066, n=3-4 mice. All
405 data shown as mean ± s.e.m.. Scale bar 5 µm.

406 (I) Low magnification image showing laminar C3 deposition in mPFC in control/CUS mice.
407 Top panel shows C3 channel (white), bottom panel shows merged C3 (red) and DAPI (blue)
408 channels. Scale bar 50 µm.

409 (J) Quantitation (left) and representative image (right) of C3 deposition in layer 2/3 mPFC after
410 control/CUS. Analyzed by two-tailed unpaired t-test, t(8)=2.675, *p=0.0281, n=5 from 3
411 mice. All data shown as mean ± s.e.m.. Scale bar 5 µm.

412 (K) Quantitation (left) and representative image (right) of C3 deposition in layer 5 mPFC after
413 control/CUS. Analyzed by two-tailed unpaired t-test, t(8)=0.9416, p=0.3739, n=5 from 3
414 mice. All data shown as mean ± s.e.m.. Scale bar 5 µm

415

416 **Figure 2. Chronic stress causes layer-specific microglial activation and synapse loss in**
417 **mPFC.**

418 (A) Orthogonal view showing localization of lysosomal marker CD68 (red) within Iba1-positive
419 microglia (blue).

420 (B) CD68 occupancy of microglia in mPFC PrL layer 2/3. Analyzed by two-tailed unpaired t-
421 test, t(28)=2.790, **p=0.0094, n=12-18 cells from 4 mice.

422 (C) CD68 occupancy of microglia in mPFC PrL layer 5. Analyzed by two-tailed unpaired t-test,
423 t(18)=0.8727, p=0.3943, n=8-12 cells from 3-4 mice. All data shown as means ± s.e.m..

424 (D) Microglial engulfment assay. Left: Representative IHC staining of Iba1-positive microglia
425 (green) with CD68-positive lysosomes (blue) and VGlut2 (magenta), scale bar 5 µm. Right:
426 Corresponding 3D reconstruction, with inset highlighting engulfed VGlut2 within microglial
427 lysosomes. Inset scale bar 1 µm.

428 (E) VGlut2 engulfment by microglia in mPFC PrL layer 2/3. Analyzed by two-way ANOVA,
429 followed by Sidak's post-hoc test comparing means within genotype, F(1,44)=6.067,
430 p=0.0178, n=12-18 cells from 4 mice, ***p=0.0006. Data excerpted from wildtype groups in
431 Figure 6D.

432 (F) VGlut2 engulfment by microglia in mPFC PrL layer 5. Analyzed by two-way ANOVA,
433 F(1,31)=0.6694, p=0.4094, n=8-12 cells from 3-4 mice. All data shown as means ± s.e.m.
434 Data excerpted from wildtype groups in Figure 6F.

435 (G) VGlut2/PSD95 synapse density in layer 2/3 mPFC. Representative images (left) and
436 quantitation (right) of colocalized VGlut2 (magenta) and PSD95 (green) puncta. Circles
437 indicate colocalized pre- and post-synaptic puncta. Scale bar 5 µm. All data shown as mean ±
438 s.e.m. Analyzed by two-way ANOVA, followed by Sidak's post-hoc test comparing means
439 within genotype, F(1,24)=10.67, p=0.0033 (genotype x stress interaction), n=7 from 3 mice,
440 **p=0.0043. Data excerpted from wildtype groups in Figure 6C.

441 (H) VGlut2/PSD95 synapse density in layer 5 mPFC. Analyzed by two-way ANOVA,
442 F(1,21)=0.07829, p=0.7824, n=6-7 from 3 mice. Data excerpted from wildtype groups in
443 Figure 6E.

444 (I) VGlut1/PSD95 synapse density in layer 2/3 mPFC. Representative images (left) and
445 quantitation (right) of colocalized VGlut1 (magenta) and PSD95 (green) puncta. Circles
446 indicate colocalized pre- and post-synaptic puncta. Scale bar 5 µm. All data shown as mean ±
447 s.e.m. Analyzed by two-tailed unpaired t-test, t(12)=0.5547, p=0.5893, n=7 from 3 mice.

448 (J) VGlut1/PSD95 synapse density in layer 5 mPFC. Analyzed by two-tailed unpaired t-test,
449 t(10)=0.1575, p=0.8780, n=6 from 3 mice.

450 (K) VGAT/gephyrin synapse density in layer 2/3 mPFC. Representative images (left) and
451 quantitation (right) of colocalized VGAT (magenta) and gephyrin (green) puncta. Circles
452 indicate colocalized pre- and post-synaptic puncta. Scale bar 5 µm. All data shown as mean ±
453 s.e.m. Analyzed by two-tailed unpaired t-test, t(9)=0.01659, p=0.9871, n=5-6 from 3 mice.

454 (L) VGAT/gephyrin synapse density in layer 5 mPFC. Analyzed by two-tailed unpaired t-test,
455 t(7)=0.4156, p=0.6901, n=4-5 from 2-3 mice.
456 (M) Representative low-magnification image of c-fos (red) and DAPI (blue) staining in mPFC
457 after TOR working memory task. Scale bar 50 µm.
458 (N) Quantitation of c-fos-positive neurons in layer 2/3 mPFC after TOR task. Analyzed by two-
459 tailed unpaired t-test, t(30)=2.371, *p=0.0244, n=14-18 from 3-4 mice. Data shown as mean
460 ± s.e.m.

461 (O) Quantitation of c-fos-positive neurons in layer 5 mPFC after TOR task. Analyzed by two-
462 tailed unpaired t-test, t(30)=0.6996, p=0.4896, n=14-18 from 3-4 mice. Data shown as mean
463 ± s.e.m.

464

465 **Figure 3. Chronic CORT administration induces an ApoE^{high} microglia state.**

466 (A) Schematic of microglia single cell isolation, FACS, and single cell RNA sequencing process.

467 (B) UMAP plot of 35,292 microglia isolated from the cerebral cortex of control and CORT mice,
468 2 replicates per condition, n = 4 mice per replicate. In total, 5 clusters of microglia were
469 identified. The largest cluster was annotated the homeostatic cluster, while other clusters
470 were annotated by the most differentially expressed gene compared to other clusters.

471 (C) Proportion of cells in each cluster for all replicates of both control and CORT conditions.

472 (D) UMAP plots of cells from each replicate.

473

474 **Figure 4. Endocytosis-associated genes are upregulated in the ApoE^{high} microglia state.**

475 (A) UMAP plots showing expression of canonical microglial genes.

476 (B) UMAP plots showing expression of marker genes for the Apoe, Prkg1, Ccl4, and Ifitm3
477 clusters.

478 (C) Heat map showing the top genes that are upregulated in each cluster relative to all other
479 clusters.

480 (D) Volcano plot of differentially expressed genes (DEGs) of the Apoe^{hi} cluster versus the
481 homeostatic cluster. Genes with $\log_2$-fold change > 0.75 are labeled.

482 (E) Pseudotime distribution of microglia in UMAP plot, with the homeostatic cluster designated
483 as the root of the trajectory.

484 (F) Expression level of the ApoE gene in pseudotime.

485 (G) Dot plot showing top 10 biological function GO terms identified by gene set enrichment
486 analysis (GSEA) of DEGs from pseudotime analysis. GO terms are arranged in order of
487 increasing adjusted p value.

488

489 **Figure 5. Complement activation drives formation of ApoE^{high} microglia state.**

490 (A) Semi-quantitative scoring of RNAscope *in situ* hybridization for ApoE mRNA (red)
491 expression in Cx3cr1-positive microglia (green). Representative images of microglia
492 categorized into bins (0-4) based on the number of ApoE puncta/clusters per nuclei.

493 (B) Stacked bar graph showing ApoE bin distribution of microglia in layer 2/3 mPFC in WT and
494 C3$^{-/-}$ control and CORT mice, displayed as % of total cells in bin; 67-85 total cells per group
495 from 2-3 mice per group.

496 (C) Stacked bar graph showing ApoE bin distribution of microglia in layer 5/6 mPFC in WT and
497 C3$^{-/-}$ control and CORT mice, displayed as % of total cells in bin; 58-85 total cells per group
498 from 2-3 mice per group.

499 (D) Bar graph showing percentage of microglia within each ApoE bin category for each genotype
500 in layer 2/3.

501 (E) Bar graph showing percentage of microglia within each ApoE bin category for each genotype
502 in layer 5/6.

503

504 **Figure 6. C3$^{-/-}$ mice are protected from stress-induced synapse loss.**

505 (A) Representative images of VGlut2 (magenta) and PSD95 (green) synapses colocalization in
506 layer 2/3 mPFC from wildtype and C3$^{-/-}$ control/CORT mice. Circles indicate colocalized
507 pre- and postsynaptic puncta. Scale bar 5 µm.

508 (B) Representative images of microglial VGlut2 synapse engulfment in layer 2/3 mPFC from
509 wildtype and C3$^{-/-}$ control/CORT mice. Representative IHC image (left) with corresponding
510 3D reconstruction (inset, right) showing localization of engulfed VGlut2 (magenta) in CD68-
511 positive lysosomes (blue) in Iba1-positive microglia (green). Scale bar 5 µm for IHC image,
512 scale bar 1 µm for inset.

513 (C) Quantitation of colocalized VGlut2 & PSD95 synaptic puncta in layer 2/3 mPFC of wildtype
514 and C3$^{-/-}$ control/CORT mice. Data analyzed by two-way ANOVA, followed by Sidak's
515 post-hoc test comparing means within genotype. $F(1,24)=10.67$, $p=0.0033$ (genotype x stress
516 interaction), n=7 from 3 mice, **p=0.0043. Data plotted as mean ± s.e.m.

517 (D) Quantitation of microglial VGlut2 engulfment in layer 2/3 mPFC of wildtype and C3$^{-/-}$ mice.
518 Data analyzed by two-way ANOVA, followed by Sidak's post-hoc test comparing means
519 within genotype, $F(1,44)=6.067$, $p=0.0178$ (genotype x stress interaction), n=12-18 cells
520 from 4 mice, ***p=0.0006. Data plotted as mean ± s.e.m.

521 (E) Quantitation of colocalized VGlut2 & PSD95 synaptic puncta in layer 5 mPFC of wildtype
522 and C3$^{-/-}$ control/CORT mice. Data analyzed by two-way ANOVA, $F(1,21)=0.07829$,
523 $p=0.7824$, n=6-7 from 3 mice. Data plotted as mean ± s.e.m.

524 (F) Quantitation of microglial VGlut2 engulfment in layer 5 mPFC of wildtype and C3$^{-/-}$ mice.
525 Data analyzed by two-way ANOVA, $F(1,31)=0.6694$, $p=0.4094$, n=8-12 cells from 3-4 mice.
526 Data plotted as mean ± s.e.m.

527

528 **Figure 7. C3$^{-/-}$ mice are protected from stress-induced behavioral deficits.**

529 (A) Timeline of CORT administration and behavioral assays (temporal object recognition "TOR"
530 and sucrose preference test "SPT").

531 (B) Schematic diagram of TOR assay (left), with image of 3D printed objects used for assay
532 (right).

533 (C) Quantitation of sucrose preference of wildtype and C3$^{-/-}$ control/CORT mice. Analyzed by
534 two-way ANOVA, followed by Sidak's post-hoc test comparing means within genotype,
535 $F(1,52)=4.481$, $p=0.0391$ (genotype x stress interaction), n=12-17 per group, wildtype
536 control vs. wildtype CORT **p=0.0017, C3$^{-/-}$ control vs. C3$^{-/-}$ CORT p=0.9298. Data plotted
537 as mean ± s.e.m.

538 (D) Object exploration time during test phase of TOR. Data analyzed by three-way ANOVA,
539 followed by uncorrected Fisher's LSD test, F(1,100)=5.758, p=0.0183 (object x genotype x
540 stress interaction), n=25-27 per group, adjusted p-values: wildtype control old vs. wildtype
541 control recent **p=0.0018, wildtype CORT old vs. wildtype CORT recent p=0.8376, $C3^{-/-}$
542 control old vs. $C3^{-/-}$ control recent *p=0.0116, $C3^{-/-}$ CORT old vs. $C3^{-/-}$ CORT recent
543 ***p=0.0004. Data plotted as mean ± s.e.m.

544 (E) Bar graphs showing discrimination index of wildtype and $C3^{-/-}$ control/CORT mice,
545 quantifying relative preference for the old object. Analyzed by two-way ANOVA, followed
546 by Sidak's post-hoc test comparing means within genotype, F(1,100)=5.784, p=0.0180
547 (genotype x stress interaction), n=25-27 per group, wildtype control vs. wildtype CORT
548 *p=0.0167, $C3^{-/-}$ control vs. $C3^{-/-}$ CORT p=0.7820.

549

550 **Supplemental Figure 1. FACS gating strategy for microglia isolation before scRNA**
551 **sequencing.**

552 (A) Representative FACS plot of input cell suspension, and separation of cells from debris based
553 on forward and side scatter.

554 (B) Representative FACS plot for isolation of single cells based on side scatter.

555 (C) Representative FACS plot for isolation of single cells based on forward scatter.

556 (D) Representative FACS plot for isolation of live cells based on low DAPI staining.

557 (E) Representative FACS plot for isolation of $CD45^{high}$ microglia cells.

558 (F) Representative FACS plot for isolation of $Cx3cr1^{high}$ and $Cd11b^{high}$ microglia cells.

559 **Methods**

560 **Animal care**

561 All animal work was approved by the UT Health Institutional Animal Care and Use Committee
562 (IACUC). Colonies were maintained in climate-controlled rooms within the AAALAC-
563 accredited UT Health animal facility. Mice were group-housed (3-4 per cage) under a 14-hour
564 light/10-hour dark cycle with ad libitum access to food and water. Clear red-tinted tunnels
565 (Bioserv, K3322) were placed in all cages for enrichment and transport purposes. To reduce
566 distress during transfer, mice were habituated to tunnel handling with daily 3-5 min tube rides for
567 1 week prior to behavioral studies. Behavioral assays were conducted either during the last 4
568 hours of the light cycle (temporal object recognition) or throughout the dark cycle (sucrose
569 preference test).

570

571 **Chronic corticosterone (CORT) stress protocol**

572 Mice received either corticosterone-infused (CORT) drinking water (Sigma 27840,
573 corticosterone dissolved at 10 mg/ml in 100% ethanol, then mixed with facility-provided
574 drinking water to a final concentration of 0.1 mg/ml corticosterone and 1% ethanol) or control
575 drinking water (1% ethanol) for 21 days, as described[54]. Both CORT and control water were
576 prepared in standard bottles using autoclaved drinking water from the animal facility and
577 replaced weekly.

578

579 **Chronic restraint stress (CRS) protocol**

580 Mice were subjected to 4 hours of restraint stress daily for 21 days, as described[54]. Restraint
581 tubes were made from 50 mL canonical tubes (Falcon, #2098) with drilled holes for air
582 circulation. Restraint tubes were placed inside the home cage. Control mice were handled twice
583 daily, 4 hours apart, for 5 minutes each. Tubes were cleaned with 70% ethanol between uses.
584

585 **Chronic unpredictable stress (CUS) protocol**

586 We used a protocol that had been shown in multiple studies to cause stress-induced circuitry
587 changes in mice[112,113]. Mice were subjected to two different stressors per day, once in the
588 morning and once in the afternoon, for 10 days. Stressors included: 15 min tail pinch, 2 hr tube
589 restraint, 30 min elevated platform, 10 min inescapable footshock (0.7mA, 2 s, 10 total shocks),
590 24 hr wet bedding with 45° cage tilt, and 24 hr light exposure. Control mice were handled twice
591 daily. CUS mice were singly housed for the duration of the stress protocol, while control mice
592 were group housed.

593

594 **Immunohistochemistry and microscopy**

595 Mice were deeply anesthetized with Avertin (0.5 mg/g) for transcardial perfusion with ice-cold
596 PBS and 4% paraformaldehyde (PFA). Brains were rapidly extracted, post-fixed for 2 hrs at 4°C
597 with gentle rocking, then cryoprotected in 30% sucrose in PBS for 48-72 hours. Brains were
598 sliced on a sliding-freezing microtome (Leica) into 20 µm sections (for synapse and complement
599 staining) or thick 40 µm sections (for microglia staining). Wash, block and antibody solutions
600 were made from PBS (pH 7.4) with either 0.15% TX-100 (0.15% PBT) or 0.3% PBT, depending
601 on slice thickness. Free-floating sections were washed 2x in PBT (10 min/wash), post-fixed in
602 4% PFA (15min) and briefly rinsed in PBS (5 min) while rocking at room temperature (RT).
603 Sections were blocked in 10% normal donkey/goat serum (Jackson Immunoresearch) at RT for 2
604 hr, then incubated in primary antibodies in 1% blocking buffer overnight at 4°C with gentle
605 rocking. Once equilibrated to RT, sections were washed 4x (10 min/wash), then incubated in
606 secondary for 2 hr. Sections were washed 2x in PBT (5 min/wash), 3x in PBS (10 min/wash)
607 then floated onto glass slides. Slides were treated with TrueBlack Lipofuscin Autofluorescence
608 Quencher (Biotium, 23007), rinsed 3x in PBS (3min/wash), then cover-slipped with
609 Fluoromount-G (SouthernBiotech, 0100-01). Slides were stored in 4° and imaged within 1 week.

610 The following primary antibodies were used for staining: goat anti-C3 (1:1000, MP Biomedicals,
611 cat#: 855730), rabbit anti-Iba1 (1:500, Fuji Film, cat#: 019-19741), rat anti-CD68 (1:500, Bio-
612 Rad, cat#: MCA1957), guinea pig anti-VGlut2 (1:1000, Synaptic Systems, cat#: 135 404), rabbit
613 anti-VGlut1 (1:1000, Synaptic Systems, cat#: 135 302), mouse anti-PSD95 K28/43, IgG2a
614 (1:500, Neuromab, cat#: 75-028), guinea pig anti-VGAT (1:500, Synaptic Systems, cat#: 131
615 004), mouse anti-gephyrin, IgG1 (1:500, Synaptic systems, cat#: 147 021), rabbit anti-cFOS
616 (1:500, Synaptic systems, cat#: 226-008).

617 The following secondary antibodies were used for staining: donkey Anti-Goat IgG A488 (1:500,
618 Jackson, cat#: 705-545-147), donkey Anti-Rabbit IgG A488 (1:500, Jackson, cat#: 711-545-
619 152), cy3-AffiniPure Donkey Anti-Rat IgG H&L (1:500, Jackson, cat#: 712-165-153), goat
620 Anti-Guinea Pig IgG Polyclonal CF-488A (1:500, Biotium, cat#: 20017-1), cy5-AffiniPure
621 Donkey Anti-Guinea Pig IgG H&L (1:500, Jackson, cat#: 706-175-148), goat Anti-Rabbit IgG
622 H&L Cy5 (1:500, Abcam, cat#: ab6564), goat anti-Mouse IgG2a A555 (1:500, Thermo Fisher
623 Scientific, cat#: A-21137), goat anti Guinea Pig IgG H&L A647 (1:500, Thermo Fisher
624 Scientific, cat#: A-21450), goat anti-Mouse IgG1 A488 (1:500, Thermo Fisher Scientific, cat#:
625 A-21121).

626 Sections were imaged using a Zeiss AxioObserver inverted microscope equipped with a Zeiss
627 Apotome.2 module. Images were acquired using a Zeiss 63x/1.4 oil Plan-Apochromat objective
628 (synapse density, microglial activation and engulfment, high-resolution C3), or Zeiss 20x Plan-
629 Neofluar objective (low-magnification C3 staining). Identical imaging and analysis parameters
630 were used for each experimental group.

631

632 **Image analysis for C3 deposition and synapse densities**

633 ImageJ (NIH) was used to quantify synapse densities and C3 deposition. Individual channels
634 were first Z-projected with summation over a depth of 2 µm, followed by background
635 subtraction (8 px rolling ball radius) and gaussian filter (sigma = 0.8). The threshold was
636 empirically determined for each channel and applied consistently to all groups. Watershed was
637 applied to binarized image. For synapse density, colocalized puncta were revealed by
638 multiplying the individual pre & post-synaptic channels using the image calculator tool. The
639 Analyze Particles tool was used to quantify the number of colocalized synaptic puncta and
640 individual C3 deposits.

641

642 **Image analysis for microglial lysosome content and synapse phagocytosis**

643 Reconstructions of microglia were performed using high-resolution confocal-quality images of
644 Iba1-positive cells using Imaris Software (version 9.7.1, Bitplane, Concord MA), as previously
645 described[45,46]. Using the image processing tool, background subtraction was first performed
646 (sigma = 1 for VGlut2, CD68; sigma = 60 for Iba1), followed by the application of a gaussian
647 filter (sigma = 0.144). All surfaces were rendered with 0.1 µm smoothing. Iba1-positive cells
648 were reconstructed first, and disconnected processes were unified with the cell body to create a
649 single surface representing one cell. To render CD68, a mask was then applied to isolate the
650 CD68 signal only within the reconstructed microglia. Another mask was then applied to isolate
651 the VGlut2 signal only within the reconstructed CD68-positive lysosomes within microglia.
652 Volumes were recorded for each reconstructed surface. For microglial lysosome content, the
653 percent of CD68 occupancy within microglia was calculated using the formula: *(volume of*
654 *CD68/volume of Iba1+ cell)*100*. For microglial engulfment of VGlut2, the percent of VGlut2
655 within microglial lysosomes was calculated using the formula: *(volume of VGlut2 within*
656 *lysosome/volume of Iba1+ cell)*100*.

657

658 **Quantification of c-fos positive cells**

659 Mice were sacrificed exactly 1 hour after completion of the TOR test phase. Brain tissue was
660 collected and processed as described above with slight modifications. In short, 40 µm-thick brain
661 sections were fixed in ice-cold 100% methanol for 5 minutes, washed in 0.3% PBT for 15
662 minutes, then blocked in 1% BSA 5% NDS in 0.3% PBT for 2 hours at RT. Sections were
663 incubated in primary antibody in blocking buffer overnight (rabbit anti-c-fos, 1:1000, Synaptic
664 Systems 226-008), washed 5x with PBT, then incubated in secondary antibody (donkey anti-
665 rabbit A488, Jackson, catalog #: 711-545-152) for 2 hr at RT. Sections were imaged on a Zeiss
666 AxioObserver inverted microscope equipped with Apotome.2 module using a Zeiss 20x Plan-
667 Neofluar objective. Analysis of c-fos positive cells was automated using an ImageJ macro by
668 applying the following sequence on 200 µm x 200 µm ROIs: gaussian filter (sigma = 2),
669 threshold (1000,65535), convert to binary mask, watershed, analyze particles.

670

671 **Microglia single cell dissociation and FACS**

672 Microglia single cell dissociation was performed using the cold mechanical dissociation
673 procedure which minimizes ex vivo activation of microglia as previously described[19,65]. Brains
674 were collected from control and CORT mice after transcardiac perfusion of ice-cold HBSS, and
675 the cerebral cortices were dissected out and minced after removal of white matter. Pieces of
676 cortices were then Dounce homogenized for 20 strokes with a loose rotating pestle, and then
677 strained through a 70 µm strainer. Cells were washed and pelleted in HBSS, and then
678 resuspended in 40% Percoll. Cells were spun at 500 g in the cold for 1 hr, and the pelleted cells
679 were washed in HBSS and resuspended in FACS buffer for staining. Cell suspensions were
680 incubated with Fc block reagent (1:50 dilution) for 15 min on ice, and then the following
681 antibodies were added from a master mix: DAPI (1:10,000), Cd11b-PE (1:50), CD45-APC-Cy7
682 (1:100), Cx3cr1-APC (1:250). Cell suspensions were further incubated for 30 min on ice, and
683 then washed twice and resuspended in FACS buffer. Cells were then immediately transported to
684 the Flow Cytometry Core Facility on ice for sorting. Sorting was performed with the following
685 gating strategy (Supplementary Figure 1): whole cells versus debris (forward scatter (FSC-A) vs
686 side scatter (SSC-A)), singlets vs aggregates (SSC-H vs SSC-A, and FSC-H vs FSC-A), live vs
687 dead (DAPI vs SSC-A), $Cd45^{high}$ (APC-Cy7-CD45 vs SSC-A), $Cx3cr1^{high}$ and $Cd11b^{high}$ (APC-
688 CX3CR1 vs PE-CD11b).

689

690 **Single cell library generation and sequencing**

691 After sorting in the cold, cells were put on ice and immediately transported to the Genome
692 Sequencing Core Facility for 10X Genomics single-cell capture and sequencing with the
693 Chromium 3' library v3.1 kit, following manufacturer's instructions. Approximately 10,000 cells
694 were targeted per sample for single cell sequencing. The single cell libraries were then
695 sequenced on an Illumina NovaSeq6000 sequencer, targeting at least 500M reads per sample, for
696 an average sequencing depth of 50,000 reads per cells. Cell Ranger v7.0.1 (10X Genomics) was
697 used for sample demultiplexing, barcode processing, unique molecular identifiers filtering, gene
698 counting, and mapping to the mouse mm10-2020-A (10X Genomics) reference genome.

699

700 **scRNA-seq clustering analysis**

701 Single cell clustering analysis was performed with the R package Seurat v4.3.0[114]. For initial
702 quality filtering, genes expressed in more than 5 cells were kept. Cells with greater than 5%
703 mitochondrial gene expression or less than 2% ribosomal gene expression were then removed.
704 Lastly, cells expressing more than 2000 genes and 5000 UMIs were kept. The SCTransform v2
705 algorithm[115] from Seurat was then used to normalize the counts in each sample. Cells were then
706 filtered for doublets using the R package DoubletFinder[116], based on an expected doublet rate of
707 7.6% for 10,000 cells per channel, as specified in the manufacturer's instructions. After filtering,
708 a total of 35,292 microglia were retained for downstream analysis.

709 Cells from all samples were integrated with Canonical Correlation Analysis (CCA) with Seurat's
710 *SelectIntegrationFeatures*, *PrepSCTIntegration*, *FindIntegrationAnchors*, and *IntegrateData*
711 functions. Principal Components Analysis (PCA) was then performed for the integrated dataset,
712 and the top 20 principal components (PCs) were chosen for clustering based on an elbowplot.
713 Clustering was performed using the *FindNeighbors* function with 20 PCs, and the *FindClusters*
714 function at a resolution of 0.08. Uniform Approximation and Projection (UMAP) dimensionality
715 reduction was performed to visualize the cell clusters with the *RunUMAP* and *DimPlot* functions.
716 Marker genes for clusters were identified using the *FindAllMarkers* function with the Wilcoxon
717 rank-sum test. The top expressing genes in each cell cluster was plotted as a heat map using the
718 *DoHeatMap* function. Comparison of differentially expressed genes (DEGs) between the
719 homeostatic and ApoE^{high} clusters were performed with the *FindMarkers* function with the
720 parameter max.cells.per.ident = 3000, and the results were plotted in a volcano plot using the
721 EnhancedVolcano R package[117].

722

723 **Pseudotime trajectory analysis**

724 The R package Monocle3[118] was used to construct a pseudotime trajectory in the clustered
725 dataset and to identify genes that were differentially expressed along the pseudotime trajectory.
726 The *learn_graph* function of Monocle3 was used to fit a principal graph in the combined dataset,
727 and the *order_cells* function was used to order the cells into trajectory along the principal graph,
728 with graph nodes in the homeostatic cluster specified as the root of the trajectory. Genes that
729 were differentially expressed along the pseudotime trajectory were determined using the
730 *graph_test* function.

731

732 **Gene set enrichment analysis (GSEA)**

733 The R package clusterProfiler[119] was used to perform GSEA. The list of DEGs from the
734 pseudotime trajectory analysis (log2FC > 0.25 and adjusted p value < 0.05, resulting in a total of
735 93 genes) was used as input to the *enrichGO* function of clusterProfiler with the following
736 parameters: keyType = "SYMBOL", OrgDb = org.Mm.eg.db, ont = "BP", pvalueCutoff = 0.05,
737 pAdjustMethod = "BH". The top 10 enriched biological process (BP) gene ontology (GO) terms
738 were ranked in order of increasing adjusted p value, and plotted as a dot plot.

739

740 **RNAscope ISH**

741 RNAscope™ Multiplex Fluorescent V2 assay (ACDBio, 323136) was carried out according to
742 manufacturer's instructions, with some modifications. Briefly, brains from PBS-perfused mice
743 were rapidly dissected and snap frozen in liquid nitrogen. Brains were sliced using a cryostat into
744 16um sections and adhered onto super-frost plus slides (Electron Microscopy Sciences, 71869-
745 20). Slides were kept on dry ice during slicing and then promptly stored at -80°C in a sealed box

746 until use. Immediately upon removal from the freezer, slides were plunged into fresh ice-cold 4%
747 PFA for 15 min, rinsed 2x with PBS, then dehydrated in serial dilutions of ethanol (50%, 75%,
748 100%, 100%). Slides were then air-dried for 5 min, and a PAP pen was used to create a
749 hydrophobic barrier around the tissue. For all subsequent steps, slides were moved to the HybEZ
750 Humidity Control Tray with wet humidifying paper for treatment/incubation, and washed in
751 coplin jars with gentle rocking (2 min per wash). At room temperature (RT), sections were
752 treated with hydrogen peroxide for 10 min, washed 3x in distilled water, treated with Protease IV
753 for 20 min, then washed 3x with PBS. Probes (Mm-CX3CR1-C2, cat no. 314221-C2 and ApoE-
754 C3, cat no. 313271-C3) were hybridized to tissue at 37°C for 2 hr, rinsed 3x in wash buffer, and
755 stored in 5x saline sodium citrate (5x SSC) buffer overnight at RT. Slides were rinsed 1x with
756 wash buffer before experiment continuation. Subsequent amplification & HRP steps were
757 performed according to manufacturer's instructions. HRP-C2 and HRP-C3 were labelled with
758 Opal 520 (1:750, Akoya FP1487001KT) and Opal 570 (1:1500, Akoya FP1488001KT),
759 respectively. Slides were counterstained with DAPI, cover slipped with Prolong Gold (Cell
760 Signaling Technology #9071), stored in 4°C and imaged within 1 week.

761 Images were acquired with a Zeiss AxioObserver equipped with an Apotome.2 module using a
762 Zeiss 40x Plan-Neuofluar objective. Analysis of ApoE expression was limited to CX3CR1+
763 DAPI nuclei. ApoE expression within microglia was evaluated using the ACDBio semi-
764 quantitative scoring system: "0" represents no staining or less than one dot per ten cells, "1"
765 represents one to three dots per cell, "2" represents four to nine dots per cell and none or very
766 few dot clusters, "3" represents 10 to 15 dots per cell and/or less than 10% of dots in clusters,
767 and "4" represents more than 15 dots per cell and/or more than 10% of dots in clusters. Bin
768 counts were aggregated within each experimental group (N=3-4 mice per group, 1-2 images per
769 mouse) to determine the bin distribution for each condition.

770

771 **Sucrose preference test (SPT) task**

772 Sucrose preference test was conducted using a 1% sucrose solution (Sigma S9378-1KG). Bottles
773 were made from 50 mL conical "iTubes" with low-aldehyde odor (Stellar Scientific, T50-600)
774 custom fitted with 2.5" sipper tubes (Fisher, NC1636707) and rubber stoppers (VWR, 76293-
775 684) to minimize leakage. Sucrose and control water were prepared using autoclaved drinking
776 water from the animal facility. Sucrose water and control water were sterile filtered before
777 aliquoting into conical tubes. Mice were simultaneously habituated to sucrose and control water
778 bottles for 3 consecutive days prior to testing. Bottles were switched in positions once daily to
779 avoid side preference. On the test day, mice were separated into individual housing and deprived
780 of water for the last 4 hours of the light cycle. Sucrose and water bottles were weighed at the
781 beginning and end of the dark cycle. Percent sucrose preference was calculated with the
782 following formula: *((sucrose consumption - water consumption) / total consumption) x 100*

783

Temporal Object Recognition (TOR) task

TOR was conducted in an 80 x 80 x 30 cm white acrylic open field arena, with white opaque wall inserts separating the arena into (4) 40 x 40 x 30 cm height square chambers (Conduct Science). Objects were 3D printed from natural PLA filament (3D printer files provided by Maithe Arruda-Carvalho[120]). Two types of objects were printed: steps and domes. To minimize intrinsic preference of mice for either object, both objects were made of the same material, and were designed to be equal in surface area. Objects were also tested in pilot studies to verify that mice had no intrinsic preference for either object, and counterbalanced between phase 1 and phase 2 as described below. Objects were centered midway along the inside of the external chamber walls, equidistant from the corners. To prevent movement, objects were affixed to the chamber floor using a small piece of BluTack adhesive putty (a fresh piece was used every round for every mouse). Chambers and objects were cleaned with 15% ethanol between each mouse and phase to minimize odor carryover. All equipment was cleaned with 70% ethanol at the end of the test session. Mice were habituated to each quadrant (chamber) of the arena, 5 min per chamber, for two consecutive days prior to testing. The TOR procedure consisted of three 5-minute phases (phase 1, phase 2 and test) with 1 hr inter-phase intervals. Mice were returned to home cage between phases. During phase 1, mice were placed in the arena with a pair of identical objects (either 2 steps or 2 domes). After a 1 hr delay, mice were reintroduced to the same chamber containing a different pair of identical objects for phase 2. During the test phase, mice were reintroduced to the same chamber containing one object from phase 1 (old object) and one object from phase 2 (recent object). Sessions were recorded using an infrared camera (OEM Cameras, DFK 33UX290) with a 3-8mm focal length lens (OEM Cameras, T3Z0312CS-MPIR) fixed to the ceiling directly above the arena. Videos were analyzed using Noldus Ethovision tracking software (Noldus Ethovision XT, Version 11.5). Behavioral analysis during the test phase was restricted to the first 20 s of total interaction time with objects, as previously described[120]. The object discrimination index was calculated using the following formula: *old object interaction time / total object interaction time*.

814 **References:**

815 1. Thomas, M.S.C., Davis, R., Karmiloff-Smith, A., Knowland, V.C.P., and Charman, T.
816 (2016). The over-pruning hypothesis of autism. Dev. Sci. *19*, 284–305. 10.1111/desc.12303.

817 2. State, M.W., and Šestan, N. (2012). The Emerging Biology of Autism Spectrum Disorders.
818 Science *337*, 1301–1303. 10.1126/science.1224989.

819 3. Kang, H.J., Voleti, B., Hajszan, T., Rajkowska, G., Stockmeier, C.A., Licznerski, P., Lepack,
820 A., Majik, M.S., Jeong, L.S., Banasr, M., et al. (2012). Decreased expression of synapse-
821 related genes and loss of synapses in major depressive disorder. Nat. Med. *18*, 1413–1417.
822 10.1038/nm.2886.

823 4. Feinberg, I. (1982). Schizophrenia: Caused by a fault in programmed synaptic elimination
824 during adolescence? J. Psychiatr. Res. *17*, 319–334. 10.1016/0022-3956(82)90038-3.

825 5. Garey, L.J., Ong, W.Y., Patel, T.S., Kanani, M., Davis, A., Mortimer, A.M., Barnes, T.R.,
826 and Hirsch, S.R. (1998). Reduced dendritic spine density on cerebral cortical pyramidal
827 neurons in schizophrenia. J. Neurol. Neurosurg. Psychiatry *65*, 446–453.

828 6. Selkoe, D.J. (2002). Alzheimer's disease is a synaptic failure. Science *298*, 789–791.
829 10.1126/science.1074069.

830 7. Osimo, E.F., Beck, K., Reis Marques, T., and Howes, O.D. (2019). Synaptic loss in
831 schizophrenia: a meta-analysis and systematic review of synaptic protein and mRNA
832 measures. Mol. Psychiatry *24*, 549–561. 10.1038/s41380-018-0041-5.

833 8. Holmes, S.E., Scheinost, D., Finnema, S.J., Naganawa, M., Davis, M.T., DellaGioia, N.,
834 Nabulsi, N., Matuskey, D., Angarita, G.A., Pietrzak, R.H., et al. (2019). Lower synaptic
835 density is associated with depression severity and network alterations. Nat. Commun. *10*,
836 1529. 10.1038/s41467-019-09562-7.

837 9. Duric, V., Banasr, M., Stockmeier, C.A., Simen, A.A., Newton, S.S., Overholser, J.C.,
838 Jurjus, G.J., Dieter, L., and Duman, R.S. (2013). Altered expression of synapse and
839 glutamate related genes in post-mortem hippocampus of depressed subjects. Int. J.
840 Neuropsychopharmacol. Off. Sci. J. Coll. Int. Neuropsychopharmacol. CINP *16*, 69–82.
841 10.1017/S1461145712000016.

842 10. Pickett, E.K., Rose, J., McCrory, C., McKenzie, C.-A., King, D., Smith, C., Gillingwater,
843 T.H., Henstridge, C.M., and Spires-Jones, T.L. (2018). Region-specific depletion of synaptic
844 mitochondria in the brains of patients with Alzheimer's disease. Acta Neuropathol. (Berl.)
845 *136*, 747–757. 10.1007/s00401-018-1903-2.

846 11. Arnsten, A.F.T., Woo, E., Yang, S., Wang, M., and Datta, D. (2022). Unusual Molecular
847 Regulation of Dorsolateral Prefrontal Cortex Layer III Synapses Increases Vulnerability to
848 Genetic and Environmental Insults in Schizophrenia. Biol. Psychiatry *92*, 480–490.
849 10.1016/j.biopsych.2022.02.003.

850 12. Dienel, S.J., Schoonover, K.E., and Lewis, D.A. (2022). Cognitive Dysfunction and
851 Prefrontal Cortical Circuit Alterations in Schizophrenia: Developmental Trajectories. Biol.
852 Psychiatry, S0006-3223(22)01072-1. 10.1016/j.biopsych.2022.03.002.

853 13. Kolluri, N., Sun, Z., Sampson, A.R., and Lewis, D.A. (2005). Lamina-specific reductions in
854 dendritic spine density in the prefrontal cortex of subjects with schizophrenia. Am. J.
855 Psychiatry *162*, 1200–1202. 10.1176/appi.ajp.162.6.1200.

856 14. Glantz, L.A., and Lewis, D.A. (2000). Decreased dendritic spine density on prefrontal
857 cortical pyramidal neurons in schizophrenia. Arch. Gen. Psychiatry *57*, 65–73.

858 15. Qiao, H., Li, M.-X., Xu, C., Chen, H.-B., An, S.-C., and Ma, X.-M. (2016). Dendritic Spines
859 in Depression: What We Learned from Animal Models. Neural Plast. *2016*.
860 10.1155/2016/8056370.

861 16. Duman, C.H., and Duman, R.S. (2015). Spine synapse remodeling in the pathophysiology
862 and treatment of depression. Neurosci. Lett. *601*, 20–29. 10.1016/j.neulet.2015.01.022.

863 17. Stogsdill, J.A., Kim, K., Binan, L., Farhi, S.L., Levin, J.Z., and Arlotta, P. (2022). Pyramidal
864 neuron subtype diversity governs microglia states in the neocortex. Nature, 1–7.
865 10.1038/s41586-022-05056-7.

866 18. Li, Q., Cheng, Z., Zhou, L., Darmanis, S., Neff, N.F., Okamoto, J., Gulati, G., Bennett, M.L.,
867 Sun, L.O., Clarke, L.E., et al. (2019). Developmental Heterogeneity of Microglia and Brain
868 Myeloid Cells Revealed by Deep Single-Cell RNA Sequencing. Neuron *101*, 207-223.e10.
869 10.1016/j.neuron.2018.12.006.

870 19. Hammond, T.R., Dufort, C., Dissing-Olesen, L., Giera, S., Young, A., Wysoker, A., Walker,
871 A.J., Gergits, F., Segel, M., Nemesh, J., et al. (2019). Single-Cell RNA Sequencing of
872 Microglia throughout the Mouse Lifespan and in the Injured Brain Reveals Complex Cell-
873 State Changes. Immunity *50*, 253-271.e6. 10.1016/j.immuni.2018.11.004.

874 20. Tan, Y.-L., Yuan, Y., and Tian, L. (2020). Microglial regional heterogeneity and its role in
875 the brain. Mol. Psychiatry *25*, 351–367. 10.1038/s41380-019-0609-8.

876 21. Keren-Shaul, H., Spinrad, A., Weiner, A., Matcovitch-Natan, O., Dvir-Szternfeld, R.,
877 Ulland, T.K., David, E., Baruch, K., Lara-Astaiso, D., Toth, B., et al. (2017). A Unique
878 Microglia Type Associated with Restricting Development of Alzheimer's Disease. Cell *169*,
879 1276-1290.e17. 10.1016/j.cell.2017.05.018.

880 22. Mathys, H., Davila-Velderrain, J., Peng, Z., Gao, F., Mohammadi, S., Young, J.Z., Menon,
881 M., He, L., Abdurrob, F., Jiang, X., et al. (2019). Single-cell transcriptomic analysis of
882 Alzheimer's disease. Nature *570*, 332–337. 10.1038/s41586-019-1195-2.

883 23. Olah, M., Menon, V., Habib, N., Taga, M.F., Ma, Y., Yung, C.J., Cimpean, M., Khairallah,
884 A., Coronas-Samano, G., Sankowski, R., et al. (2020). Single cell RNA sequencing of
885 human microglia uncovers a subset associated with Alzheimer's disease. Nat. Commun. *11*,
886 6129. 10.1038/s41467-020-19737-2.

887 24. Krasemann, S., Madore, C., Cialic, R., Baufeld, C., Calcagno, N., El Fatimy, R., Beckers, L.,
888 O'Loughlin, E., Xu, Y., Fanek, Z., et al. (2017). The TREM2-APOE Pathway Drives the
889 Transcriptional Phenotype of Dysfunctional Microglia in Neurodegenerative Diseases.
890 Immunity *47*, 566-581.e9. 10.1016/j.immuni.2017.08.008.

891 25. Absinta, M., Maric, D., Gharagozloo, M., Garton, T., Smith, M.D., Jin, J., Fitzgerald, K.C.,
892 Song, A., Liu, P., Lin, J.-P., et al. (2021). A lymphocyte-microglia-astrocyte axis in chronic
893 active multiple sclerosis. Nature. 10.1038/s41586-021-03892-7.

894 26. Tansley, S., Uttam, S., Ureña Guzmán, A., Yaqubi, M., Pacis, A., Parisien, M., Deamond,
895 H., Wong, C., Rabau, O., Brown, N., et al. (2022). Single-cell RNA sequencing reveals time-
896 and sex-specific responses of mouse spinal cord microglia to peripheral nerve injury and
897 links ApoE to chronic pain. Nat. Commun. *13*, 843. 10.1038/s41467-022-28473-8.

898 27. Wang, S., Sudan, R., Peng, V., Zhou, Y., Du, S., Yuede, C.M., Lei, T., Hou, J., Cai, Z.,
899 Cella, M., et al. (2022). TREM2 drives microglia response to amyloid-β via SYK-dependent
900 and -independent pathways. Cell *185*, 4153-4169.e19. 10.1016/j.cell.2022.09.033.

901 28. Ennerfelt, H., Frost, E.L., Shapiro, D.A., Holliday, C., Zengeler, K.E., Voithofer, G., Bolte,
902 A.C., Lammert, C.R., Kulas, J.A., Ulland, T.K., et al. (2022). SYK coordinates
903 neuroprotective microglial responses in neurodegenerative disease. Cell, S0092-
904 8674(22)01249-1. 10.1016/j.cell.2022.09.030.

905 29. Yin, Z., Herron, S., Silveira, S., Kleemann, K., Gauthier, C., Mallah, D., Cheng, Y., Margeta,
906 M.A., Pitts, K.M., Barry, J.-L., et al. (2023). Identification of a protective microglial state
907 mediated by miR-155 and interferon-γ signaling in a mouse model of Alzheimer's disease.
908 Nat. Neurosci., 1–12. 10.1038/s41593-023-01355-y.

909 30. Kaya, T., Mattugini, N., Liu, L., Ji, H., Cantuti-Castelvetri, L., Wu, J., Schifferer, M., Groh,
910 J., Martini, R., Besson-Girard, S., et al. (2022). CD8+ T cells induce interferon-responsive
911 oligodendrocytes and microglia in white matter aging. Nat. Neurosci., 1–12.
912 10.1038/s41593-022-01183-6.

913 31. Hammen, C. (2005). Stress and depression. Annu. Rev. Clin. Psychol. *1*, 293–319.
914 10.1146/annurev.clinpsy.1.102803.143938.

915 32. McEwen, B.S., and Akil, H. (2020). Revisiting the Stress Concept: Implications for
916 Affective Disorders. J. Neurosci. *40*, 12–21. 10.1523/JNEUROSCI.0733-19.2019.

917 33. Smoller, J.W. (2016). The Genetics of Stress-Related Disorders: PTSD, Depression, and
918 Anxiety Disorders. Neuropsychopharmacology *41*, 297–319. 10.1038/npp.2015.266.

919 34. Parker, K.J., Schatzberg, A.F., and Lyons, D.M. (2003). Neuroendocrine aspects of
920 hypercortisolism in major depression. Horm. Behav. *43*, 60–66. 10.1016/s0018-
921 506x(02)00016-8.

922 35. Qin, D.-D., Rizak, J., Feng, X.-L., Yang, S.-C., Lü, L.-B., Pan, L., Yin, Y., and Hu, X.-T.
923 (2016). Prolonged secretion of cortisol as a possible mechanism underlying stress and
924 depressive behaviour. Sci. Rep. *6*, 30187. 10.1038/srep30187.

925 36. Lee, B.K., Glass, T.A., McAtee, M.J., Wand, G.S., Bandeen-Roche, K., Bolla, K.I., and
926 Schwartz, B.S. (2007). Associations of salivary cortisol with cognitive function in the
927 Baltimore memory study. Arch. Gen. Psychiatry *64*, 810–818. 10.1001/archpsyc.64.7.810.

928 37. Pulopulos, M.M., Hidalgo, V., Almela, M., Puig-Perez, S., Villada, C., and Salvador, A.
929 (2014). Hair cortisol and cognitive performance in healthy older people.
930 Psychoneuroendocrinology *44*, 100–111. 10.1016/j.psyneuen.2014.03.002.

931 38. Geerlings, M.I., Sigurdsson, S., Eiriksdottir, G., Garcia, M.E., Harris, T.B., Gudnason, V.,
932 and Launer, L.J. (2015). Salivary cortisol, brain volumes, and cognition in community-
933 dwelling elderly without dementia. Neurology *85*, 976–983.
934 10.1212/WNL.0000000000001931.

935 39. Echouffo-Tcheugui, J.B., Conner, S.C., Himali, J.J., Maillard, P., DeCarli, C.S., Beiser, A.S.,
936 Vasan, R.S., and Seshadri, S. (2018). Circulating cortisol and cognitive and structural brain
937 measures: The Framingham Heart Study. Neurology *91*, e1961–e1970.
938 10.1212/WNL.0000000000006549.

939 40. Yirmiya, R., Rimmerman, N., and Reshef, R. (2015). Depression as a Microglial Disease.
940 Trends Neurosci. *38*, 637–658. 10.1016/j.tins.2015.08.001.

941 41. Wohleb, E.S., Terwilliger, R., Duman, C.H., and Duman, R.S. (2018). Stress-Induced
942 Neuronal Colony Stimulating Factor 1 Provokes Microglia-Mediated Neuronal Remodeling
943 and Depressive-like Behavior. Biol. Psychiatry *83*, 38–49. 10.1016/j.biopsych.2017.05.026.

944 42. Zhang, M.-M., Guo, M.-X., Zhang, Q.-P., Chen, X.-Q., Li, N.-Z., Liu, Q., Cheng, J., Wang,
945 S.-L., Xu, G.-H., Li, C.-F., et al. (2022). IL-1R/C3aR signaling regulates synaptic pruning in
946 the prefrontal cortex of depression. Cell Biosci. *12*, 90. 10.1186/s13578-022-00832-4.

947 43. Wang, J., Chen, H.-S., Li, H.-H., Wang, H.-J., Zou, R.-S., Lu, X.-J., Wang, J., Nie, B.-B.,
948 Wu, J.-F., Li, S., et al. (2022). Microglia-dependent excessive synaptic pruning leads to
949 cortical underconnectivity and behavioral abnormality following chronic social defeat stress
950 in mice. Brain. Behav. Immun. 10.1016/j.bbi.2022.12.019.

951 44. Crider, A., Feng, T., Pandya, C.D., Davis, T., Nair, A., Ahmed, A.O., Baban, B., Turecki, G.,
952 and Pillai, A. (2018). Complement component 3a receptor deficiency attenuates chronic
953 stress-induced monocyte infiltration and depressive-like behavior. Brain. Behav. Immun. *70*,
954 246–256. 10.1016/j.bbi.2018.03.004.

955 45. Schafer, D.P., Lehrman, E.K., Kautzman, A.G., Koyama, R., Mardinly, A.R., Yamasaki, R.,
956 Ransohoff, R.M., Greenberg, M.E., Barres, B.A., and Stevens, B. (2012). Microglia sculpt
957 postnatal neural circuits in an activity and complement-dependent manner. Neuron *74*, 691–
958 705. 10.1016/j.neuron.2012.03.026.

959 46. Cong, Q., Soteros, B.M., Wollet, M., Kim, J.H., and Sia, G.-M. (2020). The endogenous
960 neuronal complement inhibitor SRPX2 protects against complement-mediated synapse
961 elimination during development. Nat. Neurosci. *23*, 1067–1078. 10.1038/s41593-020-0672-
962 0.

963 47. Stevens, B., Allen, N.J., Vazquez, L.E., Howell, G.R., Christopherson, K.S., Nouri, N.,
964 Micheva, K.D., Mehalow, A.K., Huberman, A.D., Stafford, B., et al. (2007). The classical
965 complement cascade mediates CNS synapse elimination. Cell *131*, 1164–1178.

966 48. Arnsten, A.F.T. (2009). Stress signalling pathways that impair prefrontal cortex structure and
967 function. Nat. Rev. Neurosci. *10*, 410–422. 10.1038/nrn2648.

968 49. Haykin, H., and Rolls, A. (2021). The neuroimmune response during stress: A physiological
969 perspective. Immunity *54*, 1933–1947. 10.1016/j.immuni.2021.08.023.

970 50. Shoji, H., and Miyakawa, T. (2020). Differential effects of stress exposure via two types of
971 restraint apparatuses on behavior and plasma corticosterone level in inbred male
972 BALB/cAJcl mice. Neuropsychopharmacol. Rep. *40*, 73–84. 10.1002/npr2.12093.

973 51. Gong, S., Miao, Y.-L., Jiao, G.-Z., Sun, M.-J., Li, H., Lin, J., Luo, M.-J., and Tan, J.-H.
974 (2015). Dynamics and Correlation of Serum Cortisol and Corticosterone under Different
975 Physiological or Stressful Conditions in Mice. PLOS ONE *10*, e0117503.
976 10.1371/journal.pone.0117503.

977 52. Ding, J.X., Rudak, P.T., Inoue, W., and Haeryfar, S.M.M. (2021). Physical restraint mouse
978 models to assess immune responses under stress with or without habituation. STAR Protoc.
979 *2*, 100838. 10.1016/j.xpro.2021.100838.

980 53. Wellman, C.L. (2001). Dendritic reorganization in pyramidal neurons in medial prefrontal
981 cortex after chronic corticosterone administration. J. Neurobiol. *49*, 245–253.
982 10.1002/neu.1079.

983 54. Moda-Sava, R.N., Murdock, M.H., Parekh, P.K., Fetcho, R.N., Huang, B.S., Huynh, T.N.,
984 Witztum, J., Shaver, D.C., Rosenthal, D.L., Alway, E.J., et al. (2019). Sustained rescue of
985 prefrontal circuit dysfunction by antidepressant-induced spine formation. Science *364*,
986 eaat8078. 10.1126/science.aat8078.

987 55. Anderson, R.M., Glanz, R.M., Johnson, S.B., Miller, M.M., Romig-Martin, S.A., and
988 Radley, J.J. (2016). Prolonged corticosterone exposure induces dendritic spine remodeling
989 and attrition in the rat medial prefrontal cortex. J. Comp. Neurol. *524*, 3729–3746.
990 10.1002/cne.24027.

991 56. Yuen, E.Y., Wei, J., Liu, W., Zhong, P., Li, X., and Yan, Z. (2012). Repeated Stress Causes
992 Cognitive Impairment by Suppressing Glutamate Receptor Expression and Function in
993 Prefrontal Cortex. Neuron *73*, 962–977. 10.1016/j.neuron.2011.12.033.

994 57. Horchar, M.J., and Wohleb, E.S. (2019). Glucocorticoid receptor antagonism prevents
995 microglia-mediated neuronal remodeling and behavioral despair following chronic
996 unpredictable stress. Brain. Behav. Immun. *81*, 329–340. 10.1016/j.bbi.2019.06.030.

997 58. Chen, C.-C., Lu, J., Yang, R., Ding, J.B., and Zuo, Y. (2018). Selective activation of
998 parvalbumin interneurons prevents stress-induced synapse loss and perceptual defects. Mol.
999 Psychiatry *23*, 1614–1625. 10.1038/mp.2017.159.

1000 59. Liston, C., and Gan, W.-B. (2011). Glucocorticoids are critical regulators of dendritic spine
1001 development and plasticity in vivo. Proc. Natl. Acad. Sci. *108*, 16074–16079.
1002 10.1073/pnas.1110444108.

1003 60. Cong, Q., Soteros, B.M., Huo, A., Li, Y., Tenner, A.J., and Sia, G.M. (2022). C1q and
1004 SRPX2 regulate microglia mediated synapse elimination during early development in the
1005 visual thalamus but not the visual cortex. Glia *70*, 451–465. 10.1002/glia.24114.

1006 61. Bolkan, S.S., Stujenske, J.M., Parnaudeau, S., Spellman, T.J., Rauffenbart, C., Abbas, A.I.,
1007 Harris, A.Z., Gordon, J.A., and Kellendonk, C. (2017). Thalamic projections sustain
1008 prefrontal activity during working memory maintenance. Nat. Neurosci. *20*, 987–996.
1009 10.1038/nn.4568.

1010 62. Schmitt, L.I., Wimmer, R.D., Nakajima, M., Happ, M., Mofakham, S., and Halassa, M.M.
1011 (2017). Thalamic amplification of cortical connectivity sustains attentional control. Nature
1012 *545*, 219–223. 10.1038/nature22073.

1013 63. Parnaudeau, S., O'Neill, P.-K., Bolkan, S.S., Ward, R.D., Abbas, A.I., Roth, B.L., Balsam,
1014 P.D., Gordon, J.A., and Kellendonk, C. (2013). Inhibition of mediodorsal thalamus disrupts
1015 thalamofrontal connectivity and cognition. Neuron *77*, 1151–1162.
1016 10.1016/j.neuron.2013.01.038.

1017 64. Jett, J.D., Bulin, S.E., Hatherall, L.C., McCartney, C.M., and Morilak, D.A. (2017). Deficits
1018 in cognitive flexibility induced by chronic unpredictable stress are associated with impaired
1019 glutamate neurotransmission in the rat medial prefrontal cortex. Neuroscience *346*, 284–297.
1020 10.1016/j.neuroscience.2017.01.017.

1021 65. Marsh, S.E., Walker, A.J., Kamath, T., Dissing-Olesen, L., Hammond, T.R., de Soysa, T.Y.,
1022 Young, A.M.H., Murphy, S., Abdulraouf, A., Nadaf, N., et al. (2022). Dissection of
1023 artifactual and confounding glial signatures by single-cell sequencing of mouse and human
1024 brain. Nat. Neurosci. *25*, 306–316. 10.1038/s41593-022-01022-8.

1025 66. Corder, E.H., Saunders, A.M., Strittmatter, W.J., Schmechel, D.E., Gaskell, P.C., Small,
1026 G.W., Roses, A.D., Haines, J.L., and Pericak-Vance, M.A. (1993). Gene dose of
1027 apolipoprotein E type 4 allele and the risk of Alzheimer's disease in late onset families.
1028 Science *261*, 921–923. 10.1126/science.8346443.

1029 67. Strittmatter, W.J., Saunders, A.M., Schmechel, D., Pericak-Vance, M., Enghild, J., Salvesen,
1030 G.S., and Roses, A.D. (1993). Apolipoprotein E: high-avidity binding to beta-amyloid and

1031 increased frequency of type 4 allele in late-onset familial Alzheimer disease. Proc. Natl.
1032 Acad. Sci. U. S. A. *90*, 1977–1981. 10.1073/pnas.90.5.1977.

1033 68. Deming, Y., Filipello, F., Cignarella, F., Cantoni, C., Hsu, S., Mikesell, R., Li, Z., Del-
1034 Aguila, J.L., Dube, U., Farias, F.G., et al. (2019). The MS4A gene cluster is a key modulator
1035 of soluble TREM2 and Alzheimer's disease risk. Sci. Transl. Med. *11*, eaau2291.
1036 10.1126/scitranslmed.aau2291.

1037 69. Festa, B.P., Siddiqi, F.H., Jimenez-Sanchez, M., Won, H., Rob, M., Djajadikerta, A.,
1038 Stamatakou, E., and Rubinsztein, D.C. (2023). Microglial-to-neuronal CCR5 signaling
1039 regulates autophagy in neurodegeneration. Neuron. 10.1016/j.neuron.2023.04.006.

1040 70. Escoubas, C.C., Dorman, L.C., Nguyen, P.T., Lagares-Linares, C., Nakajo, H., Anderson,
1041 S.R., Cuevas, B., Vainchtein, I.D., Silva, N.J., Xiao, Y., et al. (2023). Type I interferon
1042 responsive microglia shape cortical development and behavior. BioRxiv Prepr. Serv. Biol.,
1043 2021.04.29.441889. 10.1101/2021.04.29.441889.

1044 71. Kolk, S.M., and Rakic, P. (2022). Development of prefrontal cortex.
1045 Neuropsychopharmacology *47*, 41–57. 10.1038/s41386-021-01137-9.

1046 72. Petanjek, Z., Judaš, M., Šimić, G., Rašin, M.R., Uylings, H.B.M., Rakic, P., and Kostović, I.
1047 (2011). Extraordinary neoteny of synaptic spines in the human prefrontal cortex. Proc. Natl.
1048 Acad. Sci. *108*, 13281–13286. 10.1073/pnas.1105108108.

1049 73. Velmeshev, D., Schirmer, L., Jung, D., Haeussler, M., Perez, Y., Mayer, S., Bhaduri, A.,
1050 Goyal, N., Rowitch, D.H., and Kriegstein, A.R. (2019). Single-cell genomics identifies cell
1051 type–specific molecular changes in autism. Science *364*, 685–689. 10.1126/science.aav8130.

1052 74. Rogers, J., and Morrison, J.H. (1985). Quantitative morphology and regional and laminar
1053 distributions of senile plaques in Alzheimer's disease. J. Neurosci. Off. J. Soc. Neurosci. *5*,
1054 2801–2808. 10.1523/JNEUROSCI.05-10-02801.1985.

1055 75. Pearson, R.C., Esiri, M.M., Hiorns, R.W., Wilcock, G.K., and Powell, T.P. (1985).
1056 Anatomical correlates of the distribution of the pathological changes in the neocortex in
1057 Alzheimer disease. Proc. Natl. Acad. Sci. U. S. A. *82*, 4531–4534. 10.1073/pnas.82.13.4531.

1058 76. Duyckaerts, C., Hauw, J.-J., Bastenaire, F., Piette, F., Poulain, C., Rainsard, V., Javoy-Agid,
1059 F., and Berthaux, P. (1986). Laminar distribution of neocortical senile plaques in senile
1060 dementia of the alzheimer type. Acta Neuropathol. (Berl.) *70*, 249–256.
1061 10.1007/BF00686079.

1062 77. Marutle, A., Gillberg, P.-G., Bergfors, A., Yu, W., Ni, R., Nennesmo, I., Voytenko, L., and
1063 Nordberg, A. (2013). ^{3}H-deprenyl and ^{3}H-PIB autoradiography show different laminar
1064 distributions of astroglia and fibrillar β-amyloid in Alzheimer brain. J. Neuroinflammation
1065 *10*, 90. 10.1186/1742-2094-10-90.

1066 78. Bayraktar, O.A., Bartels, T., Holmqvist, S., Kleshchevnikov, V., Martirosyan, A.,
1067 Polioudakis, D., Ben Haim, L., Young, A.M.H., Batiuk, M.Y., Prakash, K., et al. (2020).

1068 Astrocyte layers in the mammalian cerebral cortex revealed by a single-cell in situ
1069 transcriptomic map. Nat. Neurosci. *23*, 500–509. 10.1038/s41593-020-0602-1.

1070 79. Yin, C., Ackermann, S., Ma, Z., Mohanta, S.K., Zhang, C., Li, Y., Nietzsche, S.,
1071 Westermann, M., Peng, L., Hu, D., et al. (2019). ApoE attenuates unresolvable inflammation
1072 by complex formation with activated C1q. Nat. Med. *25*, 496–506. 10.1038/s41591-018-
1073 0336-8.

1074 80. Zhou, J., Wade, S.D., Graykowski, D., Xiao, M.-F., Zhao, B., Giannini, L.A.A., Hanson,
1075 J.E., van Swieten, J.C., Sheng, M., Worley, P.F., et al. (2023). The neuronal pentraxin Nptx2
1076 regulates complement activity and restrains microglia-mediated synapse loss in
1077 neurodegeneration. Sci. Transl. Med. *15*, eadf0141. 10.1126/scitranslmed.adf0141.

1078 81. Anastasiades, P.G., and Carter, A.G. (2021). Circuit organization of the rodent medial
1079 prefrontal cortex. Trends Neurosci. *44*, 550–563. 10.1016/j.tins.2021.03.006.

1080 82. Srinivasan, K., Friedman, B.A., Etxeberria, A., Huntley, M.A., van der Brug, M.P., Foreman,
1081 O., Paw, J.S., Modrusan, Z., Beach, T.G., Serrano, G.E., et al. (2020). Alzheimer's Patient
1082 Microglia Exhibit Enhanced Aging and Unique Transcriptional Activation. Cell Rep. *31*,
1083 107843. 10.1016/j.celrep.2020.107843.

1084 83. Frigerio, C.S., Wolfs, L., Fattorelli, N., Thrupp, N., Voytyuk, I., Schmidt, I., Mancuso, R.,
1085 Chen, W.-T., Woodbury, M.E., Srivastava, G., et al. (2019). The Major Risk Factors for
1086 Alzheimer's Disease: Age, Sex, and Genes Modulate the Microglia Response to Aβ Plaques.
1087 Cell Rep. *27*, 1293-1306.e6. 10.1016/j.celrep.2019.03.099.

1088 84. Selye, H. (1936). A Syndrome produced by Diverse Nocuous Agents. Nature *138*, 32–32.
1089 10.1038/138032a0.

1090 85. Selye, H. (1950). Stress and the general adaptation syndrome. Br. Med. J. *1*, 1383–1392.
1091 10.1136/bmj.1.4667.1383.

1092 86. Birley, J.L., and Brown, G.W. (1970). Crises and life changes preceding the onset or relapse
1093 of acute schizophrenia: clinical aspects. Br. J. Psychiatry J. Ment. Sci. *116*, 327–333.
1094 10.1192/bjp.116.532.327.

1095 87. Nuechterlein, K.H., Dawson, M.E., Ventura, J., Gitlin, M., Subotnik, K.L., Snyder, K.S.,
1096 Mintz, J., and Bartzokis, G. (1994). The vulnerability/stress model of schizophrenic relapse:
1097 a longitudinal study. Acta Psychiatr. Scand. Suppl. *382*, 58–64. 10.1111/j.1600-
1098 0447.1994.tb05867.x.

1099 88. Mohr, D.C., Hart, S.L., Julian, L., Cox, D., and Pelletier, D. (2004). Association between
1100 stressful life events and exacerbation in multiple sclerosis: a meta-analysis. BMJ *328*, 731.
1101 10.1136/bmj.38041.724421.55.

1102 89. Sotiropoulos, I., Catania, C., Pinto, L.G., Silva, R., Pollerberg, G.E., Takashima, A., Sousa,
1103 N., and Almeida, O.F.X. (2011). Stress Acts Cumulatively To Precipitate Alzheimer's

1104 Disease-Like Tau Pathology and Cognitive Deficits. J. Neurosci. *31*, 7840–7847.
1105 10.1523/JNEUROSCI.0730-11.2011.

1106 90. Harvanek, Z.M., Fogelman, N., Xu, K., and Sinha, R. (2021). Psychological and biological
1107 resilience modulates the effects of stress on epigenetic aging. Transl. Psychiatry *11*, 1–9.
1108 10.1038/s41398-021-01735-7.

1109 91. Madore, C., Yin, Z., Leibowitz, J., and Butovsky, O. (2020). Microglia, Lifestyle Stress, and
1110 Neurodegeneration. Immunity *52*, 222–240. 10.1016/j.immuni.2019.12.003.

1111 92. Sekar, A., Bialas, A.R., de Rivera, H., Davis, A., Hammond, T.R., Kamitaki, N., Tooley, K.,
1112 Presumey, J., Baum, M., Van Doren, V., et al. (2016). Schizophrenia risk from complex
1113 variation of complement component 4. Nature *530*, 177–183. 10.1038/nature16549.

1114 93. Hong, S., Beja-Glasser, V.F., Nfonoyim, B.M., Frouin, A., Li, S., Ramakrishnan, S., Merry,
1115 K.M., Shi, Q., Rosenthal, A., Barres, B.A., et al. (2016). Complement and microglia mediate
1116 early synapse loss in Alzheimer mouse models. Science *352*, 712–716.
1117 10.1126/science.aad8373.

1118 94. Shi, Q., Chowdhury, S., Ma, R., Le, K.X., Hong, S., Caldarone, B.J., Stevens, B., and
1119 Lemere, C.A. (2017). Complement C3 deficiency protects against neurodegeneration in aged
1120 plaque-rich APP/PS1 mice. Sci. Transl. Med. *9*, eaaf6295. 10.1126/scitranslmed.aaf6295.

1121 95. Hammond, J.W., Bellizzi, M.J., Ware, C., Qiu, W.Q., Saminathan, P., Li, H., Luo, S., Ma,
1122 S.A., Li, Y., and Gelbard, H.A. (2020). Complement-dependent synapse loss and
1123 microgliosis in a mouse model of multiple sclerosis. Brain. Behav. Immun.
1124 10.1016/j.bbi.2020.03.004.

1125 96. Werneburg, S., Jung, J., Kunjamma, R.B., Ha, S.-K., Luciano, N.J., Willis, C.M., Gao, G.,
1126 Biscola, N.P., Havton, L.A., Crocker, S.J., et al. (2020). Targeted Complement Inhibition at
1127 Synapses Prevents Microglial Synaptic Engulfment and Synapse Loss in Demyelinating
1128 Disease. Immunity *52*, 167-182.e7. 10.1016/j.immuni.2019.12.004.

1129 97. Bourel, J., Planche, V., Dubourdieu, N., Oliveira, A., Séré, A., Ducourneau, E.-G., Tible, M.,
1130 Maitre, M., Lesté-Lasserre, T., Nadjar, A., et al. (2021). Complement C3 mediates early
1131 hippocampal neurodegeneration and memory impairment in experimental multiple sclerosis.
1132 Neurobiol. Dis. *160*, 105533. 10.1016/j.nbd.2021.105533.

1133 98. Sellgren, C.M., Sheridan, S.D., Gracias, J., Xuan, D., Fu, T., and Perlis, R.H. (2017). Patient-
1134 specific models of microglia-mediated engulfment of synapses and neural progenitors. Mol.
1135 Psychiatry *22*, 170–177. 10.1038/mp.2016.220.

1136 99. Yilmaz, M., Yalcin, E., Presumey, J., Aw, E., Ma, M., Whelan, C.W., Stevens, B.,
1137 McCarroll, S.A., and Carroll, M.C. (2021). Overexpression of schizophrenia susceptibility
1138 factor human complement C4A promotes excessive synaptic loss and behavioral changes in
1139 mice. Nat. Neurosci. *24*, 214–224. 10.1038/s41593-020-00763-8.

1140 100. Hellewell, S.C., Welton, T., Maller, J.J., Lyon, M., Korgaonkar, M.S., Koslow, S.H.,
1141 Williams, L.M., Rush, A.J., Gordon, E., and Grieve, S.M. (2019). Profound and reproducible
1142 patterns of reduced regional gray matter characterize major depressive disorder. Transl.
1143 Psychiatry *9*, 1–8. 10.1038/s41398-019-0512-8.

1144 101. Hibar, D.P., Westlye, L.T., Doan, N.T., Jahanshad, N., Cheung, J.W., Ching, C.R.K.,
1145 Versace, A., Bilderbeck, A.C., Uhlmann, A., Mwangi, B., et al. (2018). Cortical
1146 abnormalities in bipolar disorder: an MRI analysis of 6503 individuals from the ENIGMA
1147 Bipolar Disorder Working Group. Mol. Psychiatry *23*, 932–942. 10.1038/mp.2017.73.

1148 102. Grieve, S.M., Korgaonkar, M.S., Koslow, S.H., Gordon, E., and Williams, L.M. (2013).
1149 Widespread reductions in gray matter volume in depression. NeuroImage Clin. *3*, 332–339.
1150 10.1016/j.nicl.2013.08.016.

1151 103. Gur, R.E., Turetsky, B.I., Bilker, W.B., and Gur, R.C. (1999). Reduced Gray Matter
1152 Volume in Schizophrenia. Arch. Gen. Psychiatry *56*, 905–911. 10.1001/archpsyc.56.10.905.

1153 104. Segal, A., Parkes, L., Aquino, K., Kia, S.M., Wolfers, T., Franke, B., Hoogman, M.,
1154 Beckmann, C.F., Westlye, L.T., Andreassen, O.A., et al. (2023). Regional, circuit and
1155 network heterogeneity of brain abnormalities in psychiatric disorders. Nat. Neurosci., 1–17.
1156 10.1038/s41593-023-01404-6.

1157 105. Opel, N., Goltermann, J., Hermesdorf, M., Berger, K., Baune, B.T., and Dannlowski, U.
1158 (2020). Cross-Disorder Analysis of Brain Structural Abnormalities in Six Major Psychiatric
1159 Disorders: A Secondary Analysis of Mega- and Meta-analytical Findings From the
1160 ENIGMA Consortium. Biol. Psychiatry *88*, 678–686. 10.1016/j.biopsych.2020.04.027.

1161 106. Holz, N.E., Zabihi, M., Kia, S.M., Monninger, M., Aggensteiner, P.-M., Siehl, S., Floris,
1162 D.L., Bokde, A.L.W., Desrivières, S., Flor, H., et al. (2023). A stable and replicable neural
1163 signature of lifespan adversity in the adult brain. Nat. Neurosci., 1–10. 10.1038/s41593-023-
1164 01410-8.

1165 107. Bethlehem, R. a. I., Seidlitz, J., White, S.R., Vogel, J.W., Anderson, K.M., Adamson, C.,
1166 Adler, S., Alexopoulos, G.S., Anagnostou, E., Areces-Gonzalez, A., et al. (2022). Brain
1167 charts for the human lifespan. Nature, 1–11. 10.1038/s41586-022-04554-y.

1168 108. Brouwer, R.M., Klein, M., Grasby, K.L., Schnack, H.G., Jahanshad, N., Teeuw, J.,
1169 Thomopoulos, S.I., Sprooten, E., Franz, C.E., Gogtay, N., et al. (2022). Genetic variants
1170 associated with longitudinal changes in brain structure across the lifespan. Nat. Neurosci. *25*,
1171 421–432. 10.1038/s41593-022-01042-4.

1172 109. Huttenlocher, P.R. (1979). Synaptic density in human frontal cortex - developmental
1173 changes and effects of aging. Brain Res. *163*, 195–205.

1174 110. Rakic, P., Bourgeois, J.P., Eckenhoff, M.F., Zecevic, N., and Goldman-Rakic, P.S.
1175 (1986). Concurrent overproduction of synapses in diverse regions of the primate cerebral
1176 cortex. Science *232*, 232–235. 10.1126/science.3952506.

1177 111. Harris, C.L., Heurich, M., Cordoba, S.R. de, and Morgan, B.P. (2012). The complotype:
1178 dictating risk for inflammation and infection. Trends Immunol. *33*, 513–521.
1179 10.1016/j.it.2012.06.001.

1180 112. Lei, Y., Wang, J., Wang, D., Li, C., Liu, B., Fang, X., You, J., Guo, M., and Lu, X.-Y.
1181 (2020). SIRT1 in forebrain excitatory neurons produces sexually dimorphic effects on
1182 depression-related behaviors and modulates neuronal excitability and synaptic transmission
1183 in the medial prefrontal cortex. Mol. Psychiatry *25*, 1094–1111. 10.1038/s41380-019-0352-
1184 1.

1185 113. Zhu, X., Tang, H.-D., Dong, W.-Y., Kang, F., Liu, A., Mao, Y., Xie, W., Zhang, X., Cao,
1186 P., Zhou, W., et al. (2021). Distinct thalamocortical circuits underlie allodynia induced by
1187 tissue injury and by depression-like states. Nat. Neurosci. *24*, 542–553. 10.1038/s41593-021-
1188 00811-x.

1189 114. Stuart, T., Butler, A., Hoffman, P., Hafemeister, C., Papalexi, E., Mauck, W.M., Hao, Y.,
1190 Stoeckius, M., Smibert, P., and Satija, R. (2019). Comprehensive Integration of Single-Cell
1191 Data. Cell *177*, 1888-1902.e21. 10.1016/j.cell.2019.05.031.

1192 115. Choudhary, S., and Satija, R. (2022). Comparison and evaluation of statistical error
1193 models for scRNA-seq. Genome Biol. *23*, 27. 10.1186/s13059-021-02584-9.

1194 116. McGinnis, C.S., Murrow, L.M., and Gartner, Z.J. (2019). DoubletFinder: Doublet
1195 Detection in Single-Cell RNA Sequencing Data Using Artificial Nearest Neighbors. Cell
1196 Syst. *8*, 329-337.e4. 10.1016/j.cels.2019.03.003.

1197 117. Blighe, K., Rana, S., and Lewis, M. (2018). EnhancedVolcano: publication-ready
1198 volcano plots with enhanced colouring and labeling.

1199 118. Trapnell, C., Cacchiarelli, D., Grimsby, J., Pokharel, P., Li, S., Morse, M., Lennon, N.J.,
1200 Livak, K.J., Mikkelsen, T.S., and Rinn, J.L. (2014). The dynamics and regulators of cell fate
1201 decisions are revealed by pseudotemporal ordering of single cells. Nat. Biotechnol. *32*, 381–
1202 386. 10.1038/nbt.2859.

1203 119. Yu, G., Wang, L.-G., Han, Y., and He, Q.-Y. (2012). clusterProfiler: an R Package for
1204 Comparing Biological Themes Among Gene Clusters. OMICS J. Integr. Biol. *16*, 284–287.
1205 10.1089/omi.2011.0118.

1206 120. Cruz-Sanchez, A., Dematagoda, S., Ahmed, R., Mohanathaas, S., Odenwald, N., and
1207 Arruda-Carvalho, M. (2020). Developmental onset distinguishes three types of spontaneous
1208 recognition memory in mice. Sci. Rep. *10*, 10612. 10.1038/s41598-020-67619-w.

1209

Figure 1

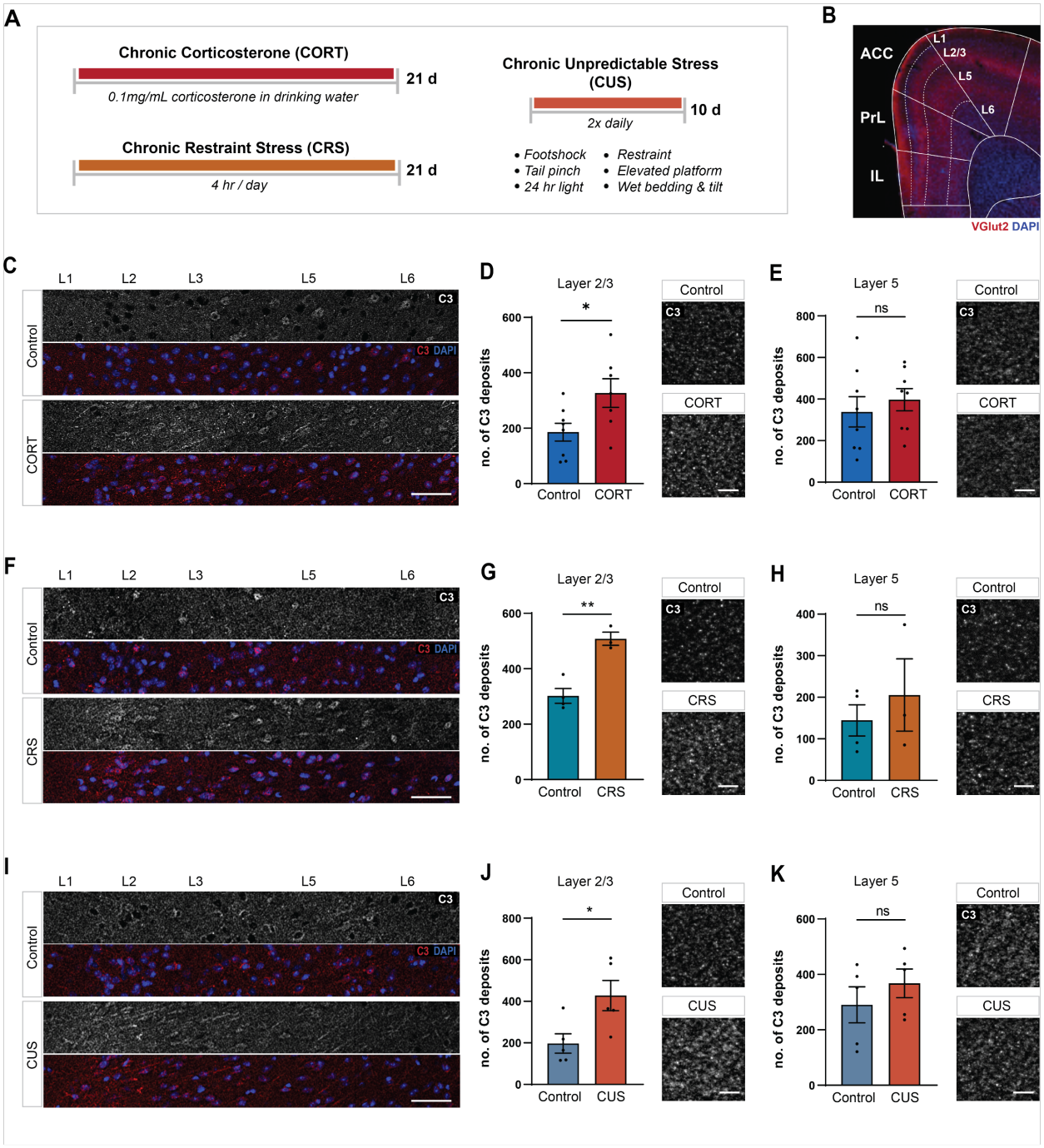
A
Chronic Corticosterone (CORT)
21 d
0.1mg/mL corticosterone in drinking water
Chronic Restraint Stress (CRS)
21 d
4 hr / day
Chronic Unpredictable Stress (CUS)
10 d
2x daily
• Footshock
• Tail pinch
• 24 hr light
• Restraint
• Elevated platform
• Wet bedding & tilt
B
ACC
PrL
IL
L1
L2/3
L5
L6
VGlut2 DAPI
C
L1
L2
L3
L5
L6
Control
CORT
C3
C3 DAPI
D
Layer 2/3
no. of C3 deposits
Control
CORT
E
Layer 5
ns
F
CRS
G
**
H
I
CUS
J
K

Figure 2

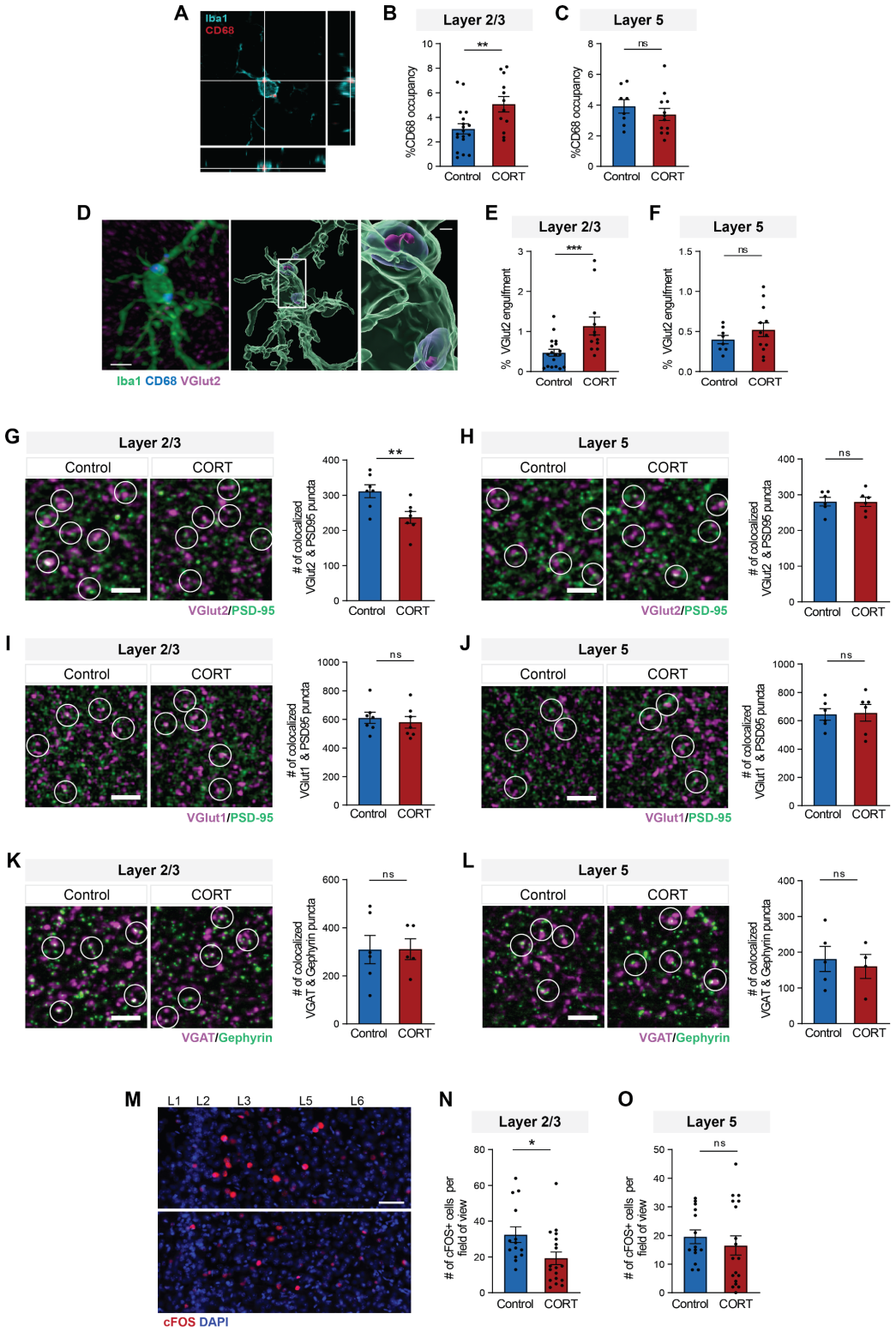
A
Iba1
CD68
B
Layer 2/3
%CD68 occupancy
Control
CORT
C
Layer 5
%CD68 occupancy
Control
CORT
D
Iba1 CD68 VGlut2
E
Layer 2/3
% VGlut2 engulfment
Control
CORT
F
Layer 5
% VGlut2 engulfment
Control
CORT
G
Layer 2/3
Control
CORT
VGlut2/PSD-95
# of colocalized VGlut2 & PSD95 puncta
H
Layer 5
Control
CORT
VGlut2/PSD-95
# of colocalized VGlut2 & PSD95 puncta
I
Layer 2/3
Control
CORT
VGlut1/PSD-95
# of colocalized VGlut1 & PSD95 puncta
J
Layer 5
Control
CORT
VGlut1/PSD-95
# of colocalized VGlut1 & PSD95 puncta
K
Layer 2/3
Control
CORT
VGAT/Gephyrin
# of colocalized VGAT & Gephyrin puncta
L
Layer 5
Control
CORT
VGAT/Gephyrin
# of colocalized VGAT & Gephyrin puncta
M
L1 L2 L3 L5 L6
cFOS DAPI
N
Layer 2/3
# of cFOS+ cells per field of view
Control
CORT
O
Layer 5
# of cFOS+ cells per field of view
Control
CORT

Figure 3

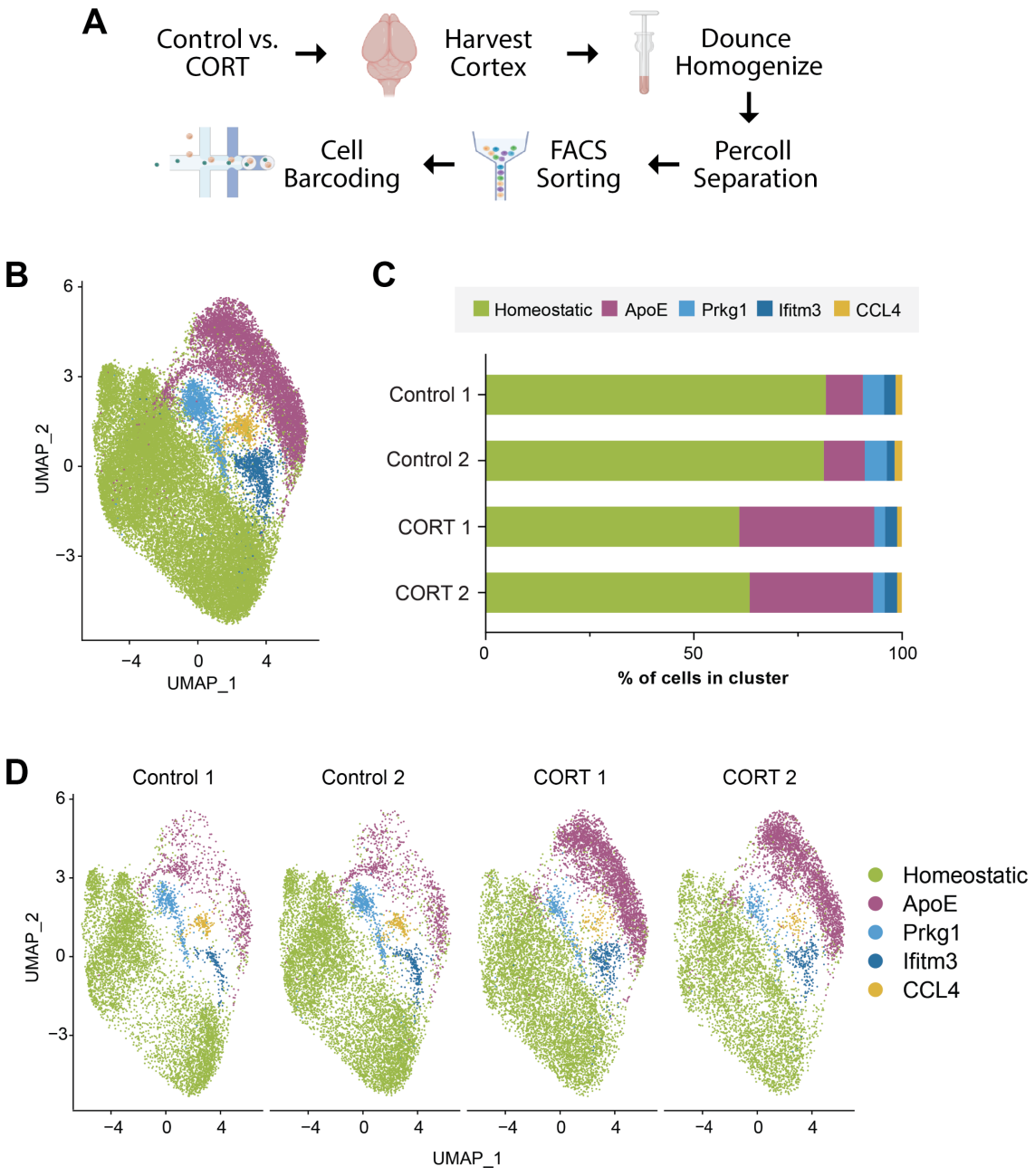
A
Control vs. CORT
Harvest Cortex
Dounce Homogenize
Percoll Separation
FACS Sorting
Cell Barcoding
B
UMAP_2
UMAP_1
C
Homeostatic
ApoE
Prkg1
Ifitm3
CCL4
Control 1
Control 2
CORT 1
CORT 2
% of cells in cluster
D
Control 1
Control 2
CORT 1
CORT 2
UMAP_2
UMAP_1
Homeostatic
ApoE
Prkg1
Ifitm3
CCL4

Figure 4

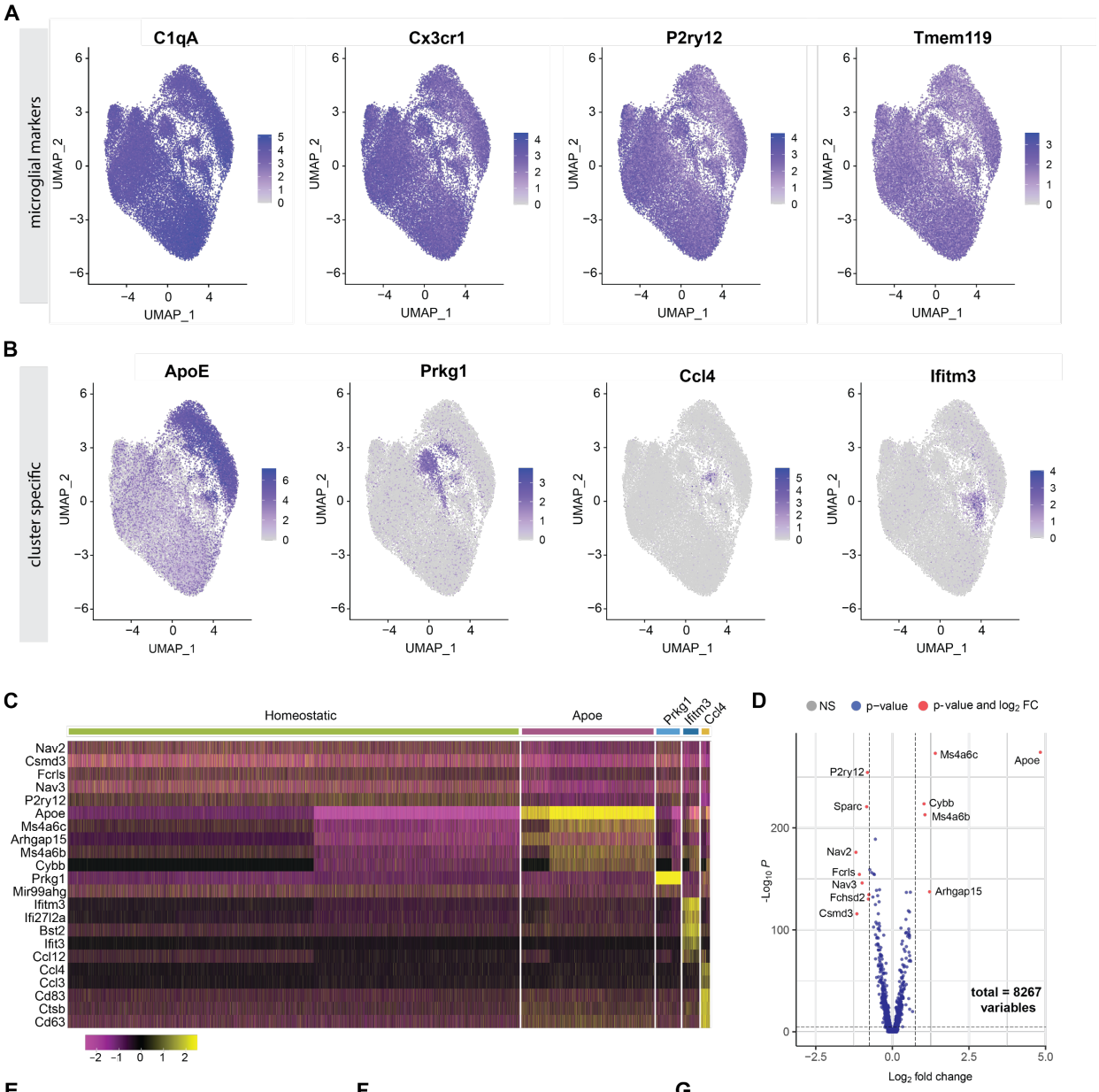
A
microglial markers
C1qA
Cx3cr1
P2ry12
Tmem119
UMAP_1
UMAP_2
B
cluster specific
ApoE
Prkg1
Ccl4
Ifitm3
C
Homeostatic
Apoe
Prkg1
Ifitm3
Ccl4
Nav2
Csmd3
Fcrls
Nav3
P2ry12
Apoe
Ms4a6c
Arhgap15
Ms4a6b
Cybb
Prkg1
Mir99ahg
Ifitm3
Ifi27l2a
Bst2
Ifit3
Ccl12
Ccl4
Ccl3
Cd83
Ctsb
Cd63
D
NS
p-value
p-value and log2 FC
Ms4a6c
Apoe
P2ry12
Sparc
Cybb
Ms4a6b
Nav2
Fcrls
Nav3
Fchsd2
Csmd3
Arhgap15
total = 8267 variables
-Log10 P
Log2 fold change
E
UMAP 1
UMAP 2
F
ApoE
Expression
pseudotime
G
receptor−mediated endocytosis
negative regulation of immune system process
negative regulation of cell activation
intrinsic apoptotic signaling pathway
myeloid cell differentiation
processing & presentation of exogenous peptide antigens
antigen processing and presentation
processing & presentation of exogenous peptide antigen
processing & presentation of peptide antigen
processing & presentation of polysaccharide antigen
via MHC class II
Count
p.adjust
GeneRatio

Figure 5

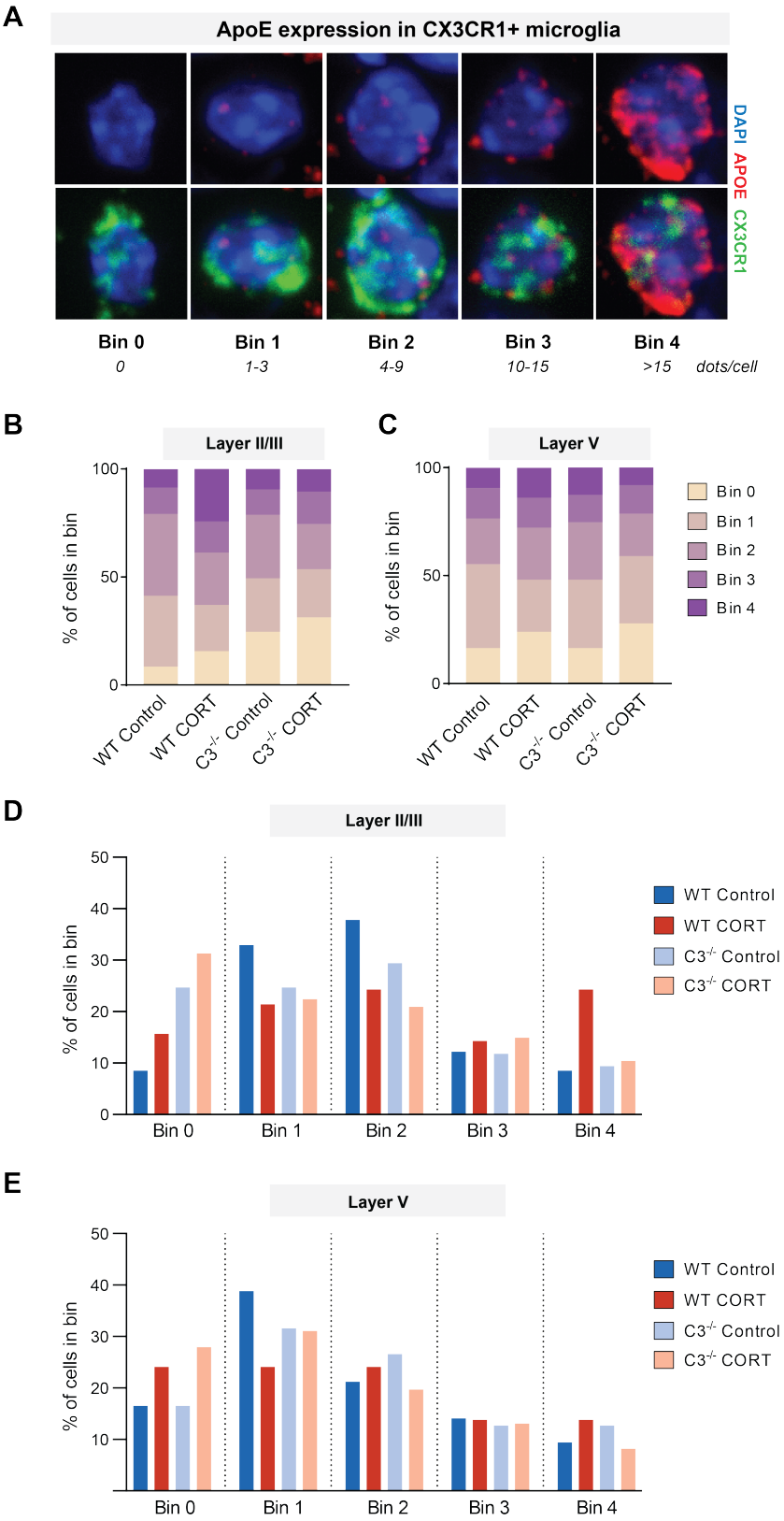
A
ApoE expression in CX3CR1+ microglia
DAPI
APOE
CX3CR1
Bin 0
0
Bin 1
1-3
Bin 2
4-9
Bin 3
10-15
Bin 4
>15
dots/cell
B
Layer II/III
% of cells in bin
100
50
0
WT Control
WT CORT
C3-/- Control
C3-/- CORT
C
Layer V
% of cells in bin
100
50
0
WT Control
WT CORT
C3-/- Control
C3-/- CORT
Bin 0
Bin 1
Bin 2
Bin 3
Bin 4
D
Layer II/III
% of cells in bin
50
40
30
20
10
0
Bin 0
Bin 1
Bin 2
Bin 3
Bin 4
WT Control
WT CORT
C3-/- Control
C3-/- CORT
E
Layer V
% of cells in bin
50
40
30
20
10
Bin 0
Bin 1
Bin 2
Bin 3
Bin 4
WT Control
WT CORT
C3-/- Control
C3-/- CORT

Figure 6

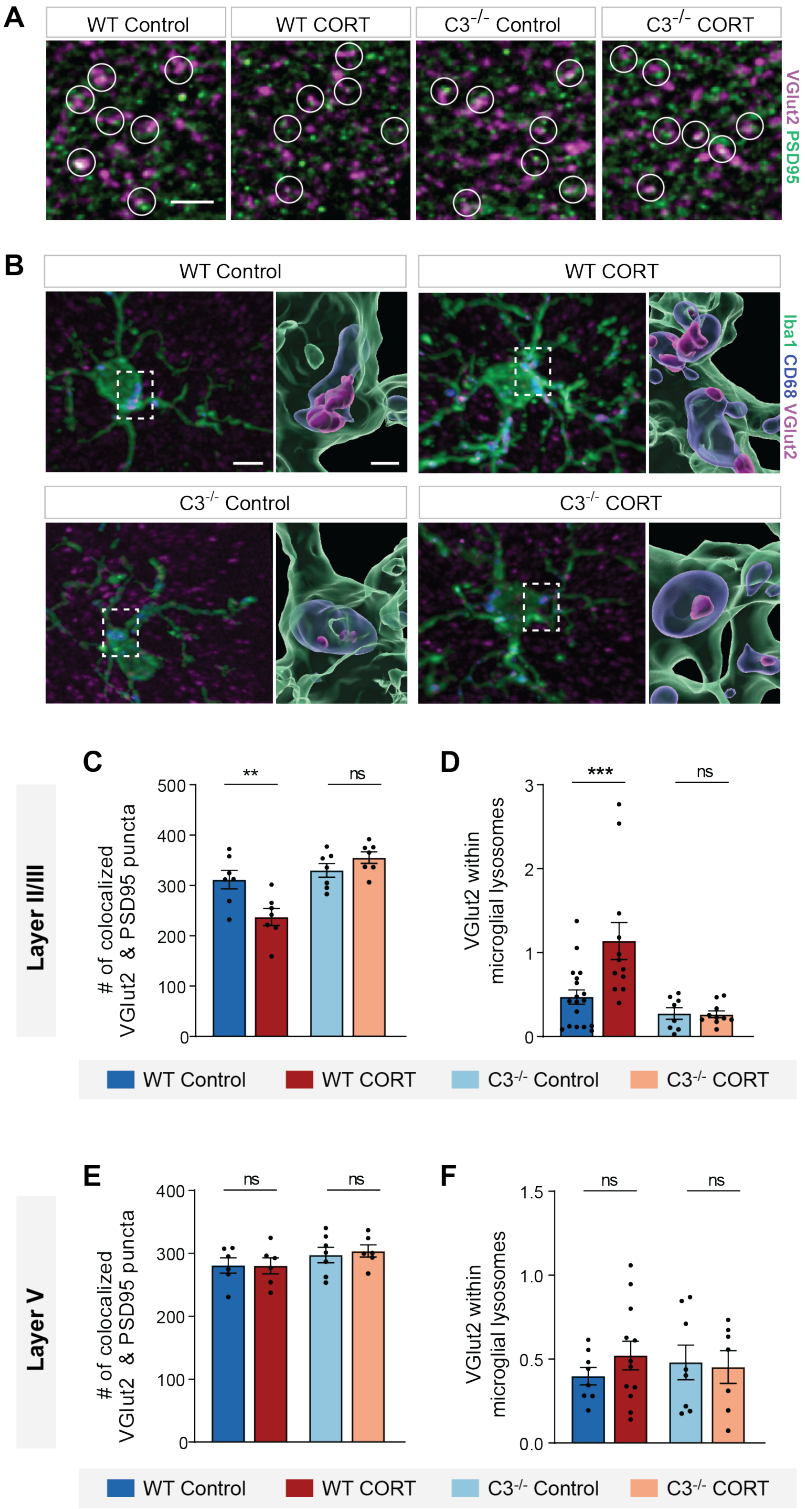
A
WT Control
WT CORT
C3-/- Control
C3-/- CORT
VGlut2 PSD95
B
WT Control
WT CORT
Iba1 CD68 VGlut2
C3-/- Control
C3-/- CORT
Layer II/III
C
# of colocalized VGlut2 & PSD95 puncta
**
ns
D
VGlut2 within microglial lysosomes
***
ns
WT Control
WT CORT
C3-/- Control
C3-/- CORT
Layer V
E
# of colocalized VGlut2 & PSD95 puncta
ns
ns
F
VGlut2 within microglial lysosomes
ns
ns
WT Control
WT CORT
C3-/- Control
C3-/- CORT

Figure 7

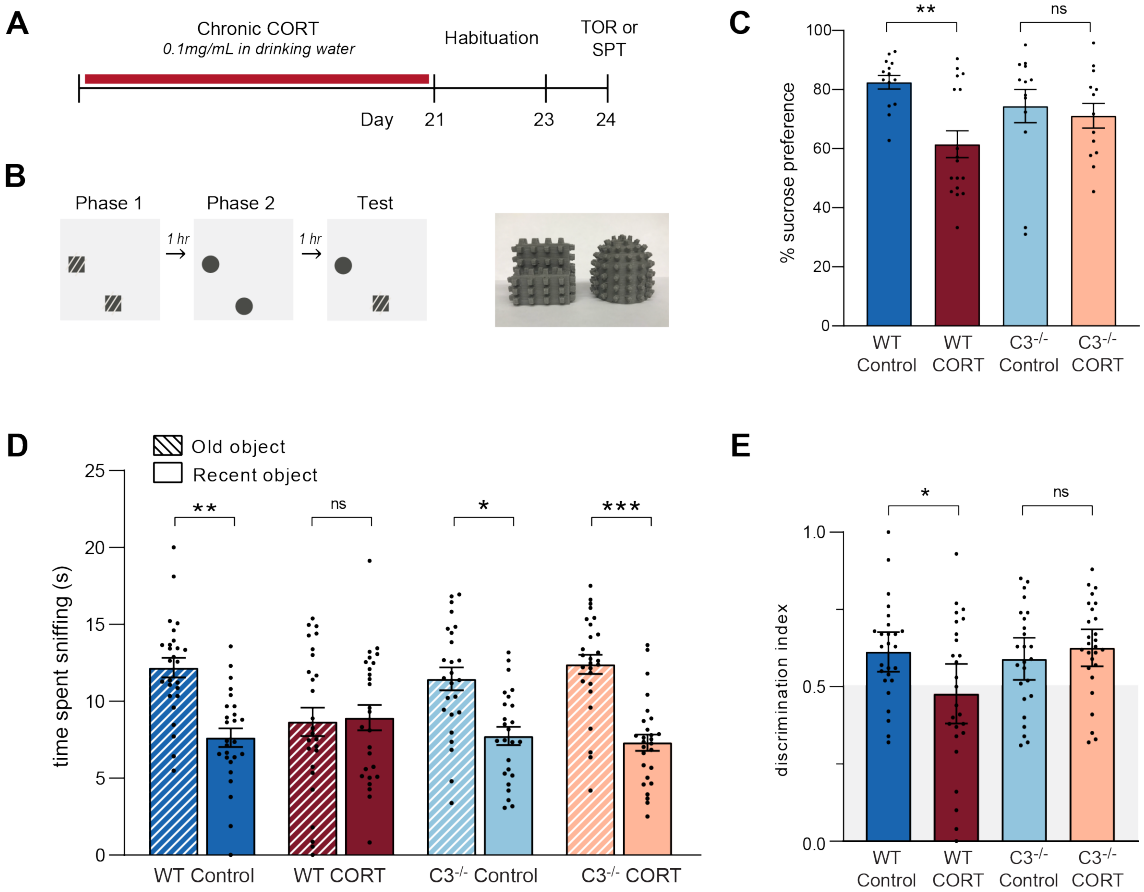
A
Chronic CORT
0.1mg/mL in drinking water
Habituation
TOR or SPT
Day
21
23
24
B
Phase 1
Phase 2
Test
1 hr
1 hr
C
% sucrose preference
100
80
60
40
20
0
**
ns
WT Control
WT CORT
C3-/- Control
C3-/- CORT
D
Old object
Recent object
time spent sniffing (s)
25
20
15
10
5
0
**
ns
*
***
WT Control
WT CORT
C3-/- Control
C3-/- CORT
E
discrimination index
1.0
0.5
0.0
*
ns
WT Control
WT CORT
C3-/- Control
C3-/- CORT
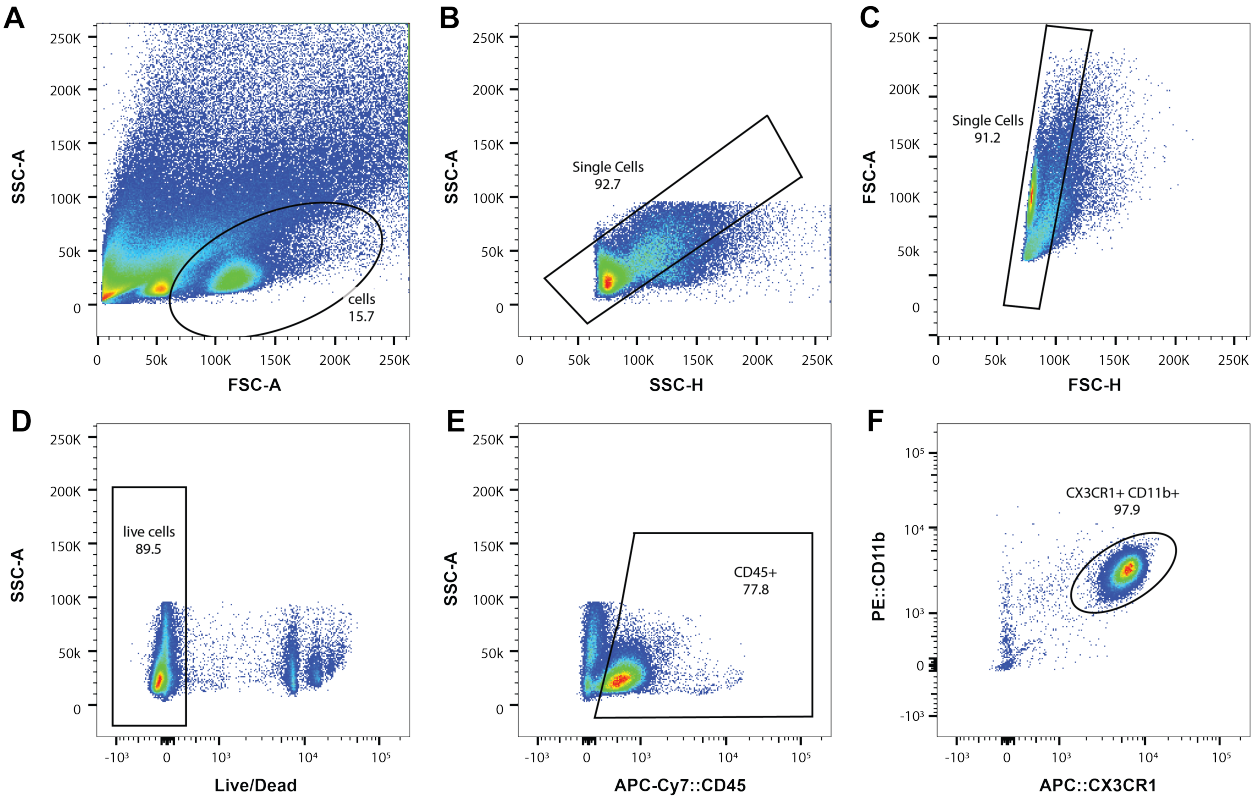
Supplementary Figure 1